JOURNAL OF GEOPHYSICAL RESEARCH, VOL. 114, F04014, doi:10.1029/2009JF001305, 2009

Quantifying canyon incision and Andean Plateau surface uplift, southwest Peru: A thermochronometer and numerical modeling approach

Taylor F. Schildgen,[1,2] Todd A. Ehlers,[3,4] David M. Whipp Jr.,[3,5] Matthijs C. van Soest,[6] Kelin X. Whipple,[6] and Kip V. Hodges[6]

Received 11 March 2009; revised 29 June 2009; accepted 11 August 2009; published 12 November 2009.

[1] Apatite and zircon (U-Th)/He ages from Ocoña canyon at the western margin of the Central Andean plateau record rock cooling histories induced by a major phase of canyon incision. We quantify the timing and magnitude of incision by integrating previously published ages from the valley bottom with 19 new sample ages from four valley wall transects. Interpretation of the incision history from cooling ages is complicated by a southwest to northeast increase in temperatures at the base of the crust due to subduction and volcanism. Furthermore, the large magnitude of incision leads to additional three-dimensional variations in the thermal field. We address these complications with finite element thermal and thermochronometer age prediction models to quantify the range of topographic evolution scenarios consistent with observed cooling ages. Comparison of 275 model simulations to observed cooling ages and regional heat flow determinations identify a best fit history with $\leq$0.2 km of incision in the forearc region prior to $\sim$14 Ma and up to 3.0 km of incision starting between 7 and 11 Ma. Incision starting at 7 Ma requires incision to end by $\sim$5.5 to 6 Ma. However, a 2.2 Ma age on a volcanic flow on the current valley floor and 5 Ma gravels on the uplifted piedmont surface together suggest that incision ended during the time span between 2.2 and 5 Ma. These additional constraints for incision end time lead to a range of best fit incision onset times between 8 and 11 Ma, which must coincide with or postdate surface uplift.

Citation: Schildgen, T. F., T. A. Ehlers, D. M. Whipp Jr., M. C. van Soest, K. X. Whipple, and K. V. Hodges (2009), Quantifying canyon incision and Andean Plateau surface uplift, southwest Peru: A thermochronometer and numerical modeling approach, *J. Geophys. Res.*, *114*, F04014, doi:10.1029/2009JF001305.

1. Introduction

[2] Low-temperature thermochronology can record changes in the near-surface thermal field within the crust in response to evolving surface topography [e.g., *Lees*, 1910; *Benfield*, 1949; *Turcotte and Schubert*, 1982; *Stüwe et al.*, 1994; *Mancktelow and Grasemann*, 1997; *Braun*, 2002a; *Ehlers and Farley*, 2003]. Such data have been used to demonstrate the antiquity and evolution of mountain topography [e.g., *House et al.*, 1998, 2001; *Ehlers et al.*, 2006; *Herman et al.*, 2007], relief change in landscapes [e.g., *Braun*, 2002a; *Braun and Robert*, 2005; *Shuster et al.*, 2005], and the timing of major canyon incision [e.g., *Clark et al.*, 2005; *Ouimet*, 2007; *Schildgen et al.*, 2007]. In many cases, precise interpretations of the data are limited by complications involving the thermal response time to changes in surface topography, lateral and/or temporal variations in crustal thermal properties, and insufficient information on surface morphology prior to major changes [e.g., *Reiners et al.*, 2005].

[3] In this paper we explore how some of these complications affect interpretations of thermochronologic data from southwest Peru, where *Schildgen et al.* [2007] used a valley bottom transect of apatite (U-Th)/He data to decipher the cooling signal induced by a major phase of canyon incision on the western margin of the Central Andean plateau. Uplift of the plateau margin resulted in a broad warping of the landscape between the margin and the coast, with erosion focused in major river valleys and only minor erosional modification of the surrounding low-relief interfluve surface. Canyon incision could either coincide with or postdate surface uplift, given that incision on the order of several kilometers in magnitude must be driven by surface uplift of at least this magnitude. However, the time required for an incision signal to propagate through

[1]Department of Earth, Atmospheric, and Planetary Sciences, Massachusetts Institute of Technology, Cambridge, Massachusetts, USA.
[2]Now at Institut für Geowissenschaften, University of Potsdam, Potsdam, Germany.
[3]Department of Geological Sciences, University of Michigan, Ann Arbor, Michigan, USA.
[4]Now at Institut für Geowissenschaften, Universität Tübingen, Tübingen, Germany.
[5]Now at Géosciences Rennes, Université de Rennes 1, Rennes, France.
[6]School of Earth and Space Exploration, Arizona State University, Tempe, Arizona, USA.

0148-0227/09/2009JF001305$09.00

a drainage system implies that the onset of incision provides only a minimum estimate for the onset of surface uplift.

[4] Early topographic growth of the Central Andes is difficult to constrain, but sedimentary units deposited in the forearc region provide some clues. The regional sedimentary package that blankets the forearc region known as the Moquegua Formation in Peru [e.g., *Sempere et al.*, 2004; *Roperch et al.*, 2006] and the Azapa Formation in northern Chile [e.g., *Wörner et al.*, 2002] consists of a thick package of siltstone and sandstone red beds that are unconformably overlain by debris flow and fluvial conglomerates. Red beds of the Lower Moquegua Formation are estimated to have been deposited starting at ~50 Ma ($^{40}Ar/^{39}Ar$ dating of biotite), and the unconformity beneath the coarser sediments is estimated to be ~30 Ma ($^{40}Ar/^{39}Ar$ dated ashes) [*Sempere et al.*, 2004; *Roperch et al.*, 2006], indicating that some inland topography existed before that time. Surface elevations probably grew to more significant heights prior to deposition of the upper Moquegua conglomerates, which are dated from ~30 to ~14 Ma based on numerous interlayered ashes [*Thouret et al.*, 2007]. Later uplift in the region is better constrained. In southern Peru, thermochronologic data and $^{40}Ar/^{39}Ar$ ages on valley-filling volcanic flows suggest that at least 2.4 km of uplift-driven incision started at ~9 to 10 Ma and ended by ~2.3 Ma [*Schildgen et al.*, 2007, 2009; *Thouret et al.*, 2007]. These results agree broadly with uplift estimates from other regions in the Central Andes. These include oxygen isotope and clumped isotope data from the Altiplano interior [*Ghosh et al.*, 2006; *Garzione et al.*, 2006; *Quade et al.*, 2007], paleobotany data [*Singewald and Berry*, 1922; *Berry*, 1939; *Graham et al.*, 2001; *Gregory-Wodzicki*, 2000], geomorphic evidence from the plateau margins [*Gubbels et al.*, 1993; *Kennan et al.*, 1997; *Barke and Lamb*, 2006; *Hoke et al.*, 2007; *Hoke and Garzione*, 2008], and structural analysis of deformed sediments [*Nester*, 2008; *Jordan et al.*, 2006], as summarized in Table 1. However, these uplift estimates are only minima or they are bracketed by large uncertainties. In the case of stable isotope data, the measured signal is also sensitive to regional climate change [e.g., *Ehlers and Poulsen*, 2009]. Placing better constraints on the magnitude of uplift during this most recent tectonic phase is of particular importance, because the development of major topographic barriers such as the Andes has important effects on local and global atmospheric circulation and precipitation patterns [e.g., *Rodwell and Hoskins*, 2001; *Takahashi and Battisti*, 2007; *Bookhagen and Strecker*, 2008]. More sophisticated analyses of low-temperature thermochronologic data from southwest Peru can provide more precise constraints on the uplift history of the western margin of the Central Andean plateau, and can better inform how topographic evolution of this region relates to development of this major orogenic plateau.

[5] We use a 3-D finite element thermal model to explore the range of topographic evolution scenarios consistent with thermochronologic data collected from the region. The model records the thermal history of rocks as they are advected to the surface through a thermal field that includes the effects of evolving surface topography, and predicts thermochronologic ages of rocks collected at the surface. We compare model results to 19 new apatite (U-Th)/He ages from four valley wall transects in addition to data previously reported by *Schildgen et al.* [2007] (12 apatite and 12 zircon (U-Th)/He ages). All apatite and zircon data are summarized in supplementary Tables S1, S2, and S3 of the auxiliary material.[1]

2. Geologic and Thermal Setting

2.1. Plateau Evolution

[6] The ~3.8 km average elevation of the Central Andes produces an effective orographic barrier to precipitation [e.g., *Alpers and Brimhall*, 1988; *Lenters and Cook*, 1995, 1997; *Houston and Hartley*, 2003; *Bookhagen and Strecker*, 2008], resulting in a close relationship between regional climate changes and the morphologic evolution of the orogen [e.g., *Strecker et al.*, 2007]. The high interior Altiplano Plateau developed through internal drainage between two flanking ranges: the Eastern and Western Cordilleras (Figure 1). The Eastern Cordillera (EC) and regions farther east experienced on the order of 300 km of shortening across a foreland-propagating fold thrust belt that tracks outward growth of the plateau [*McQuarrie*, 2002; *McQuarrie et al.*, 2008]. This included distributed deformation in the Altiplano, EC, and Interandean zone from ~40 to 20 Ma, followed by deformation in the Subandean Zone in the last ~20 Ma [e.g., *Strecker et al.*, 1989; *Gubbels et al.*, 1993; *Allmendinger and Gubbels*, 1996; *Echavarria et al.*, 2003; *Horton*, 2005; *Barnes et al.*, 2006, 2008; *Elger et al.*, 2005; *Ege et al.*, 2007]. In contrast, the Western Cordillera, marked by a line of arc volcanoes and what *Isacks* [1988] described as a crustal-scale monocline, is characterized by only ~3 km of crustal shortening that ended by ~10 Ma [e.g., *Victor et al.*, 2004; *Farías et al.*, 2005] and very low exhumation rates throughout the deformation period [e.g., *Schildgen et al.*, 2007].

2.2. Regional Geologic and Thermal Setting

[7] The long-term evolution of the subduction zone at the western margin of South America poses particular challenges to understanding the thermal evolution of this region. Changes in the thermal field through time can be related to variations in the convergence rate between the subducting Nazca plate and the South American margin since at least late Cretaceous time [e.g., *Pardo-Casas and Molnar*, 1987; *Somoza*, 1998] and related temporal changes in upper plate shortening and the dip of the descending slab [e.g., *Jordan et al.*, 1983; *Sébrier and Soler*, 1991; *Mercier et al.*, 1992; *Jaillard and Soler*, 1996]. Changes in the position of the magmatic arc are related to both changing slab dip as well as subduction erosion [e.g., *von Huene and Ranero*, 2003], although the arc is estimated to have reached its current position in Peru by ~20 Ma [*Stern*, 2004]. In northern and central Peru, oblique subduction of the Nazca Ridge is interpreted to have generated a pulse of uplift that has propagated southward down the coast but that has not yet affected southwest Peru [e.g., *Machare and Ortlieb*, 1992; *Li and Clark*, 1994; *Hampel*, 2002; *Clift et al.*, 2003]. Both the cross-strike variations in crustal temperature above the subduction zone and temporal changes in the subduction geom-

[1] Auxiliary materials are available in the HTML. doi:10.1029/2009JF001305.

Table 1. Late Cenozoic Uplift Estimates for the Central Andes

Location	Uplift Magnitude (m)	Initiation (Ma)	Method/Evidence	Reference
Corocoro, Altiplano	2000 ± 2000	~10 to 15	Paleobotany	*Singewald and Berry* [1922]
Potosi, Altiplano	3040 ± 1260	~13.8 to 20.8	Paleobotany	*Gregory-Wodzicki* [2000]
Jakokkota, Altiplano	2535 ± 1405	~10 to 11	Paleobotany	*Gregory-Wodzicki* [2000]
Callapa, Altiplano	2500–3500	~10.3	Oxygen isotopes	*Garzione et al.* [2006]
Callapa, Altiplano	3400 ± 600	~10.3	Clumped isotopes	*Ghosh et al.* [2006]
S. Peru, W. Cordillera	>2400	~9	Incised canyons	*Schildgen et al.* [2007]
S. Peru, W. Cordillera	2000–2500	~13 to 9	Incised canyons	*Thouret et al.* [2007]
N. Chile, W. Cordillera	>1000	~10	Incised canyons	*Hoke et al.* [2007]
N. Chile, W. Cordillera	~1000	~10	Incised paleosurfaces	*Hoke and Garzione* [2008]
N. Chile, W. Cordillera	>1400	~10	Rotated basin fill	*Nester* [2008]
N. Chile, W. Cordillera	250–1800	~10	Rotated lake beds	*Jordan et al.* [2006]
Potosi, E. Cordillera	1500 ± 2000	~13.8 to 20.8	Paleobotany	*Berry* [1939]
Bolivia, E. Cordillera	1950 ± 1250	~12 to 9	Incised paleosurfaces	*Kennan et al.* [1997]
Pislepampa, E. Cordillera	2300 ± 1100	~6 to 7	Paleobotany	*Graham et al.* [2001]
Bolivia, E. Cordillera	1705 ± 695	~12 to 9	Incised paleosurfaces	*Barke and Lamb* [2006]

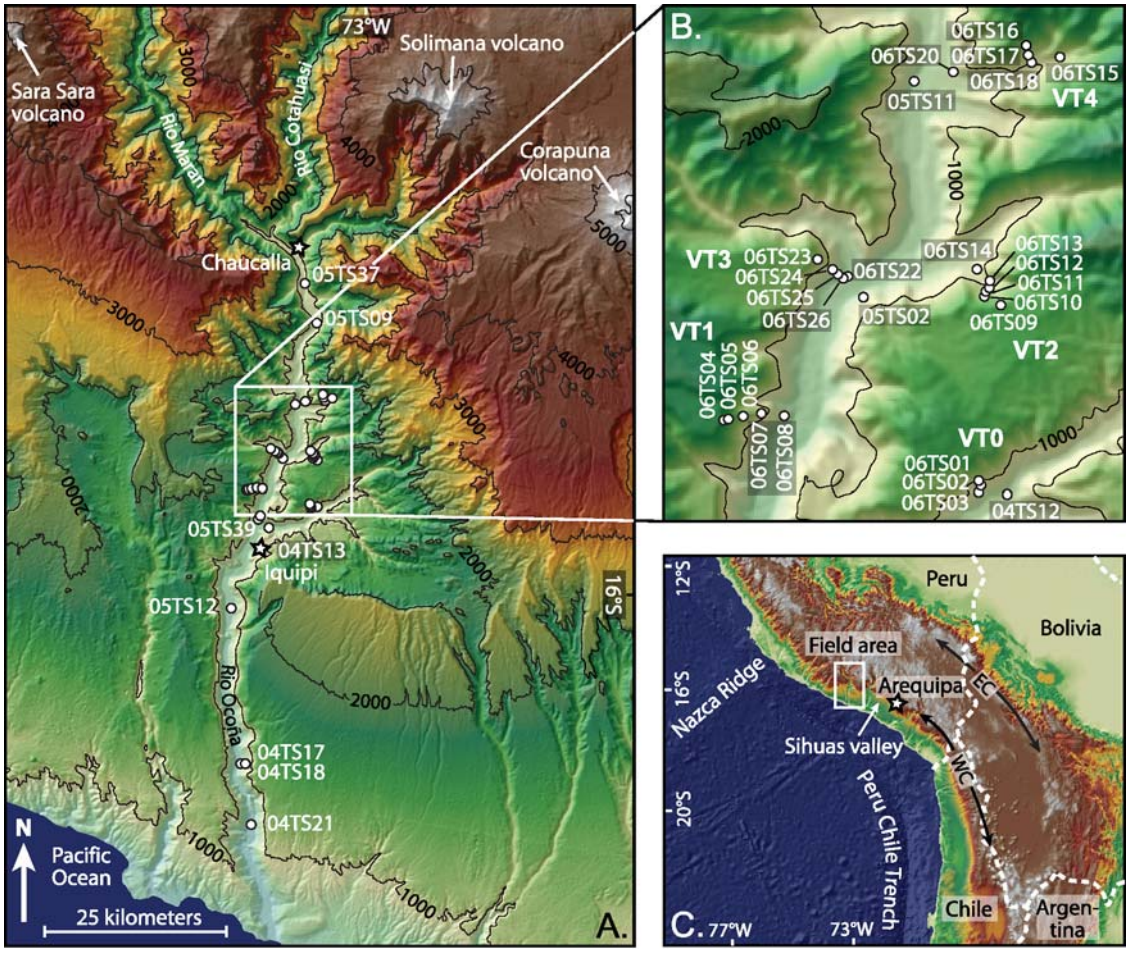

Figure 1. Location map showing Ocoña canyon in southwest Peru and thermochronologic sample sites for zircon and apatite (U-Th)/He dating. (a and b) Topography is illustrated by a 30 m resolution semitransparent DEM colored by elevation draped over a hillshade layer. The DEM was derived from Advanced Spaceborne Thermal Emission and Reflection Radiometer (ASTER) imagery. Contour interval is 1000 m. Towns are indicated with white stars. White box outlines region from which valley wall transects were collected and is shown in greater detail in Figure 1b. Overview of regional topography of the Central Andes and bathymetry of the Pacific Ocean is derived from GTOPO30 DEM data (offshore) and SRTM 90 m resolution onshore DEM data. (c) Solid white line outlines the field area, dashed white lines shows national boundaries, and black arrows indicate the position along the plateau margin of the Western Cordillera (WC) and the Eastern Cordillera (EC).

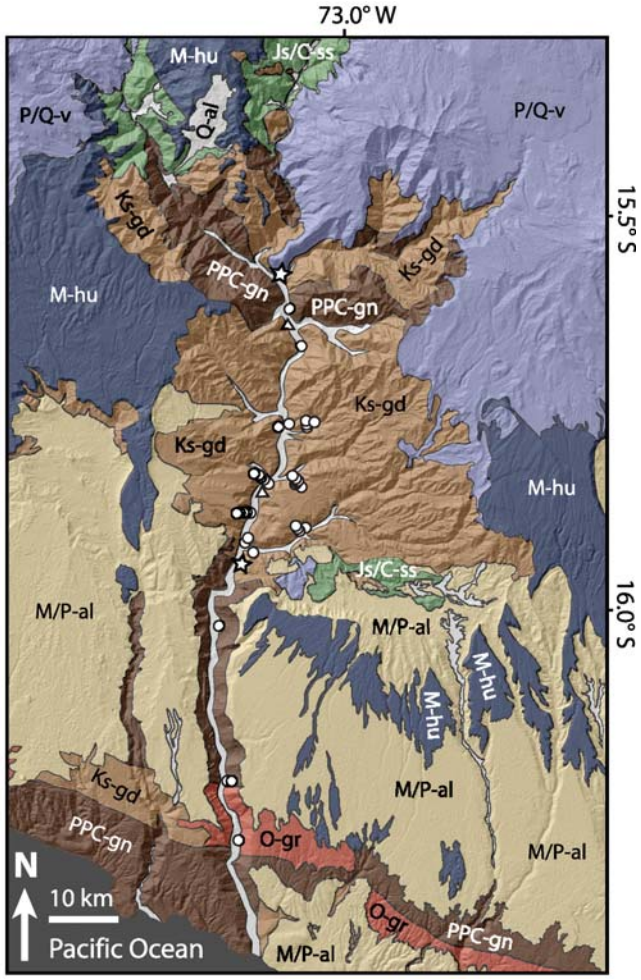

Figure 2. Simplified geologic map of Ocoña canyon based on mapping by *INGEMMET* [2001] and by *Schildgen et al.* [2009]. Dated valley-filling volcanic flows are too small to appear at the scale of mapping, but locations are shown with white triangles. White circles indicate thermochronology sample locations. PPC-gn, Precambrian gneiss; Js/C-ss, Jurassic/Cretaceous sandstone, limestone; Ks-gd, Cretaceous granodiorite, diorite, and tonalite; M/P-al, Mio-Pliocene alluvium, landslide, and marine sediments; M-hu, Miocene Huaylillas Formation ignimbrites; P/Q-v:, Plio-Quaternary extrusive volcanics; Q-al, Quaternary alluvium.

etry are important considerations for interpretations of thermochronologic data traversing a forearc region. Our study is focused on the Ocoña drainage in southwest Peru, which cuts through the active volcanic arc lining the western margin of the Central Andean plateau, and drains ~80 km through the forearc region toward the coast (Figure 1). The early thermal history of the region was likely dominated by cooling of the arc-related coastal batholith that crops out through much of the forearc region in Peru, and locally in the middle reaches of Ocoña canyon (Figure 2). Geologic maps [*INGEMMET*, 2001] identify Cretaceous diorites, tonalities, and granodiorites in this region, and new $^{40}Ar/^{39}Ar$ step-heating experiments on biotite samples from the canyon yielded ages of 137.5 ± 1.8 Ma and 135.7 ± 1.7 Ma (Table 2). Southeast of the canyon, near Arequipa, U/Pb zircon ages on similar intrusive bodies demonstrate a long-lived history of plutonism, with ages ranging from 61.0 to 188.4 Ma [*Mukasa*, 1986]. Modern-day arc volcanoes in the region form a line roughly parallel to the coast at the northeast margin of the intrusive bodies. Volcanic units derived from these centers range in age from ~24 to <1 Ma, span a radius of ~15 to 20 km surrounding the volcanoes, and in some places can be found inset along canyon walls filling paleotributary valleys [*Schildgen et al.*, 2007; *Thouret et al.*, 2007]. In the middle and lower reaches of the canyon, however, where thermochronologic samples for this study were collected, only a small number of volcanic flows entered from side valley tributaries. Although these flows are only likely to have caused significant heating in close proximity to their margins, they still may have partially reset ages on some samples, as discussed later in section 3.3.

[8] Regional variability in the crustal thermal field for the present day is recorded by surface heat flow determinations. Low values (30 to 60 mW/m^2) from coastal and forearc regions increase gradually to higher values (50 to 180 mW/m^2) on the plateau [*Henry and Pollack*, 1988; *Hamza and Munoz*, 1996; *Springer and Förster*, 1998; *Springer*, 1999; *Hamza et al.*, 2005]. Localized high heat flow anomalies are generally located within a ~10 km radius of active volcanoes, and as *Springer* [1999] noted, can be explained by magma chambers at ~4 to 6 km depth. Although no measurements have been made on volcanoes in our study area, they are potential locations for such anomalies. Even if the thermal effects of local arc volcanoes are limited, understanding the effect of spatial variation in geothermal gradients on thermochronologic ages that traverse the forearc region is difficult without explicit modeling.

2.3. Regional Climate and Geomorphology

[9] Arid to hyperarid conditions over most of this region have important implications for bedrock exhumation history. The Sechura Desert of western Peru and northernmost Chile is one of the driest regions on earth, due to the combined effects of its position in the descending flow of the atmospheric Hadley cell circulation, the cold oceanic

Table 2. $^{40}Ar/^{39}Ar$ Data Sample Description and Location

Sample	Material	Description	Weighted Age[a] (Ma)	MSWD[b]	Latitude (W)	Longitude (S)
06TS21	groundmass	Flow at present valley bottom	2.21 ± 0.02	1.62	73°06′20.07″	15°51′04.78″
04TS12	biotite	Ocoña valley intrusive rock	137 ± 1.8	5.32	73°03′14.08″	15°54′35.77″
04TS13	biotite	Ocoña valley intrusive rock	136 ± 1.7	1.77	73°07′04.58″	15°55′58.36″
07TS12	feldspar	Tuff 200m above valley floor	2.01 ± 0.03	0.59	73°06′10.15″	15°56′00.55″

[a]07TS12 and 06TS21 ages relative to TCR-2a at 28.34 Ma; 04TS12 and 04TS13 ages relative to FCT at 28.02 Ma.
[b]Mean Square Weighted Deviation.

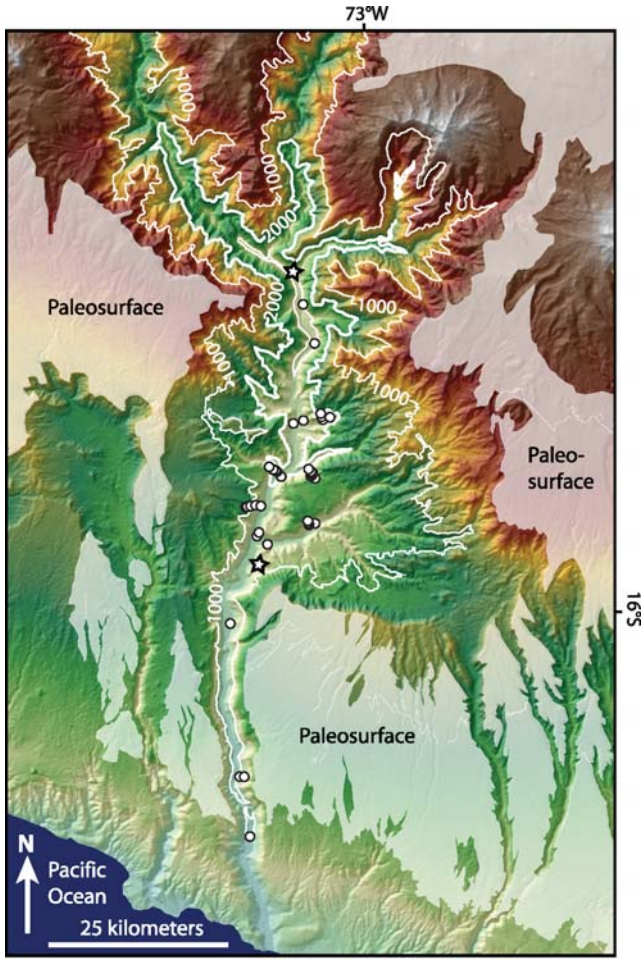

Figure 3. Map of depths below regional paleosurface. White shading indicates the relict surface over which a spline surface was fit to determine surface topography prior to surface uplift and incision. Depths of samples below the paleosurface are indicated by 1000 m contour lines. The 2000 m contour line is highlighted, as it indicates the approximate position where data plotted on age versus depths plot show a transition from shallow slopes at depths less than 2000 m to steep slopes at greater depths.

Peru (Humboldt) Current that leads to temperature inversions at the coast, and the orographic barrier created by the Andes that blocks moisture-bearing easterly winds [*Abele*, 1989]. Precipitation in southwest Peru ranges from a hyperarid 2 to 10 mm/yr near the coast, up to a semiarid 300 to 400 mm/yr in the upper catchments of major rivers [*Houston and Hartley*, 2003], leading to very slow modern exhumation rates. Studies of soil development in northern Chile suggest this dry pattern has characterized the western margin since 13 to 19 Ma, and climate was more uniformly semiarid prior to that time [*Rech et al.*, 2006]. Regional hillslope exhumation rates fall within the range of 0.001 to 0.05 mm/yr when integrated over the past ~10 to 75 million years in southern Peru [*Schildgen et al.*, 2007] and over the past 0.02 to 6 million years in northern Chile [*Kober et al.*, 2007]. This long-term, slow exhumation contrasts with rapid incision that carved major canyons in the region, which slice down over 3 km below the surrounding, slowly exhuming interfluve surfaces (Figure 3).

3. Thermochronologic Data

[10] Because of the complex nature of the thermal field in this area, new samples collected from 4 valley wall transects (Figure 1 and Tables S1–S3) along with samples collected along a valley bottom transect reported by *Schildgen et al.* [2007] are interpreted in the context of 3D thermal modeling.

3.1. Sample Preparation and Analysis

[11] Most samples were collected from Cretaceous diorites and granodiorite, although samples close to the coast were collected from gneisses and quartzites. Samples were prepared by first crushing all material to less than 500 microns using only a jaw crusher to minimize the number of cracked apatite crystals. Apatite separates were derived through use of a water table, Frantz magnetic separator, and heavy liquid density separations using bromoform. Intrusive samples yielded generally high quantities of euhedral apatite grains, and metamorphic samples yielded apatites that were slightly rounded. Euhedral apatite crystals were inspected for inclusions under 150× magnification and cross-polarized light. Inclusion-free grains that exceeded 70 microns in diameter were photographed, measured for length and average diameter, and loaded into platinum tubes as single-grain aliquots. Helium was extracted in an ASI Alphachron (U-Th)/He dating system by laser heating the samples within a vacuum chamber with a 980nm diode laser for 5 min at 9 Amps. The gas was spiked with ^{3}He and exposed to a SAES NP-10 getter for 2 min, after which the gas was expanded into a Pfeiffer – Balzers Prisma Quadrupole mass spectrometer. Currently the composition of the ^{4}He standard gas tank is known to 1.18%, which provides the largest contribution to the error in this part of the analytical process. Samples were then spiked with ^{235}U and ^{230} Th with a concentration of 15 ng/mL and 5 ng/mL, respectively, and allowed to dissolve in 50% distilled ultrapure HNO_3. The dissolved apatite solution was analyzed on a Thermo X series quadrupole in the Keck Lab at ASU. Reproducibility of the spiked standard analysis is on the order of 1.0% for U and 1.4% for Th. Ages were calculated with an iterative process (as the age equation reported by *Dodson* [1973] has no direct analytical solution for time) using blank corrected He, Th, and U values. Raw ages were corrected for alpha ejection effects following methods described in the work of *Farley et al.* [1996] and *Farley* [2002]. Analytical errors propagated throughout the process amount to 1.5–2.5% (1σ). Errors associated with the alpha ejection correction were not directly determined, but following discussions of *Farley et al.* [1996], *Spotila et al.* [1998], and *Hourigan et al.* [2005], they are estimated to push the total error for the method to 3–5% 1σ. Alpha ejection corrections were made assuming a homogeneous U and Th distribution, which may not be realistic and can lead to significant additional scatter in the age data [e.g., *Hourigan et al.*, 2005]. Additional details of the sample analysis procedure are described in the work of *Schildgen et al.* [2009]. Results for all individual crystal data and mean age calculations are provided in Tables S1–S3 of the auxiliary material.

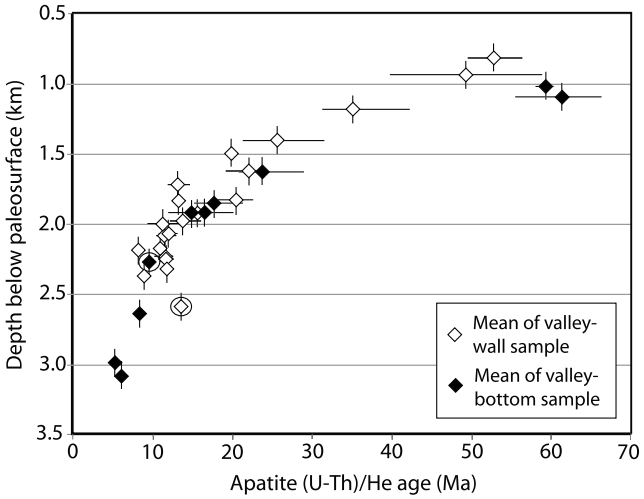

Figure 4. Apatite (U-Th)/He data from valley bottom and valley wall transects in Ocoña canyon plotted against depth beneath reconstructed paleosurface. Black diamonds show mean ages of valley bottom transect samples, and white diamonds show mean ages of each sample in four different valley wall transects (V1 through V4). The *y* axis error bars reflect an estimated ±100 m uncertainty in the depth of samples below the regional paleosurface, which was defined by fitting a spline surface across the canyon (see *Schildgen et al.* [2007] for details). The *x* axis bars show the range of individual crystal ages for each sample. Circled samples were excluded from analysis due to either proximity to a volcanic flow or suspicion that the sample was from a landslide block.

3.2. Valley Bottom Transect Data

[12] Elevation is commonly used as a proxy for distance from the closure temperature isotherm over small spatial distances or where there are no topographic features of sufficiently long wavelength to affect the shape of near-surface isotherms. In southern Peru, however, elevation is not an adequate reference frame. There, differential uplift and very slow background erosion rates created a modern topography that rises slowly from the coast to 4 km elevations over an ~80 km long transect. The shape of near-surface isotherms should mimic this paleosurface. For this reason, depth below the regional paleosurface [e.g., *Clark et al.*, 2005; *Schildgen et al.*, 2007] provides the best reference frame for comparing samples collected throughout canyons incising the forearc region. Age-elevation plots of such data, in contrast, would show patterns dominated by long-wavelength effects of topography and not accurately reflect changes in exhumation [e.g., *Huntington et al.*, 2007]. Against the regional pattern of isotherms mimicking the paleosurface, canyon incision caused local deflection of near-surface isotherms, and associated rapid cooling [*Schildgen et al.*, 2007]. Because the valley bottom data traverses a range of depths beneath the paleosurface (Figure 3), this type of sample transect is useful for deciphering the incision-induced cooling signal, but only when plotted on an age versus depth plot.

[13] Valley bottom samples were collected over a 70 km transect (Figure 1) with a range of elevations from 73 to 852 m, a corresponding range of depths below the paleosurface from 890 to 3080 m (Figure 3), and a range of apatite (U-Th)/He ages from 5.3 to 72.5 Ma. On an age versus depth plot of the apatite-He data (black diamonds in Figure 4), the steep slope shown by samples younger than ~9 Ma reflects rapid cooling, while the shallow slope in samples older than ~15 Ma reflects slow background denudation. The break in slope reflects the approximate onset time of rapid cooling. *Schildgen et al.* [2007] used the exposed thickness of the rapidly cooled zone and 1-D thermal modeling of the inferred base of the zone to estimate the total thickness of the rapidly cooled zone, which implied at least 2.4 km of post-9 Ma incision in the deepest reaches of the canyon.

[14] The conclusions in that paper assumed that lateral variations in the thermal field and in incision rates had insignificant effects on the data. Our purpose here is to further evaluate the robustness of those conclusions and refine the estimate of the timing and amount of incision in light of the strong lateral gradient in heat flow and possible effects associated with the valley incision process.

3.3. Valley Wall Transect Data

[15] We collected valley wall transects from the middle reaches of Ocoña canyon, focused around the region where the break in slope occurred in the valley bottom transect data: at depths approximately 2 km below the paleosurface (Figure 3). Transects VT1 and VT3 are from along the walls of the main valley, while VT0, VT2, and VT4 are from side valleys. The transect closest to the coast (VT1), with sample depths of 0.8 to 2.3 km, shows relatively old mean apatite (U-Th)/He ages, ranging from ~10 to 55 Ma, and a gentle slope reflecting slow background denudation of ~0.025 mm/yr (Figure 5). The middle transects, VT2 and VT3, sample depth ranges of 1.5 to 2.3 km and 1.6 to 2.3 km, and show ranges in mean ages from 8 to 20 Ma and 9 to 23 Ma, respectively. Samples from VT4, the transect farthest inland, show a range of ages between 8 and 14 Ma at depths of 2.0 to 2.7 km reflecting faster exhumation of approximately 0.1 mm/yr. In VT2 and VT3, a break in slope may occur at 11 to 15 Ma, but is not well constrained due to limited samples above the break (Figure 5).

[16] When compiled in a single plot, the valley wall transect data reveal trends similar to that seen in the valley bottom transect (white diamonds in Figure 4). Shallow samples are generally old and show a low slope (~0.025 mm/yr), reflecting slow background exhumation rates. Deeper than 2 km below the paleosurface, ages are younger and show better individual crystal reproducibility (Figure 5 and Table S1), as expected in rapidly cooled samples. They show a steep slope (~0.18 mm/yr) reflecting fast cooling due to isotherm depression in response to canyon incision. Although the valley bottom transect shows a sharp break in slope at ~9 Ma, valley wall transect data show a dispersed transition region between ~11 and 15 Ma. Apart from this, the main difference between the data sets is that the slope of the older suite of ages from the valley wall transects is steeper and better defined than that of the valley bottom transect.

[17] In our analysis, we excluded one sample that we suspected may be too close to valley-filling volcanic flows

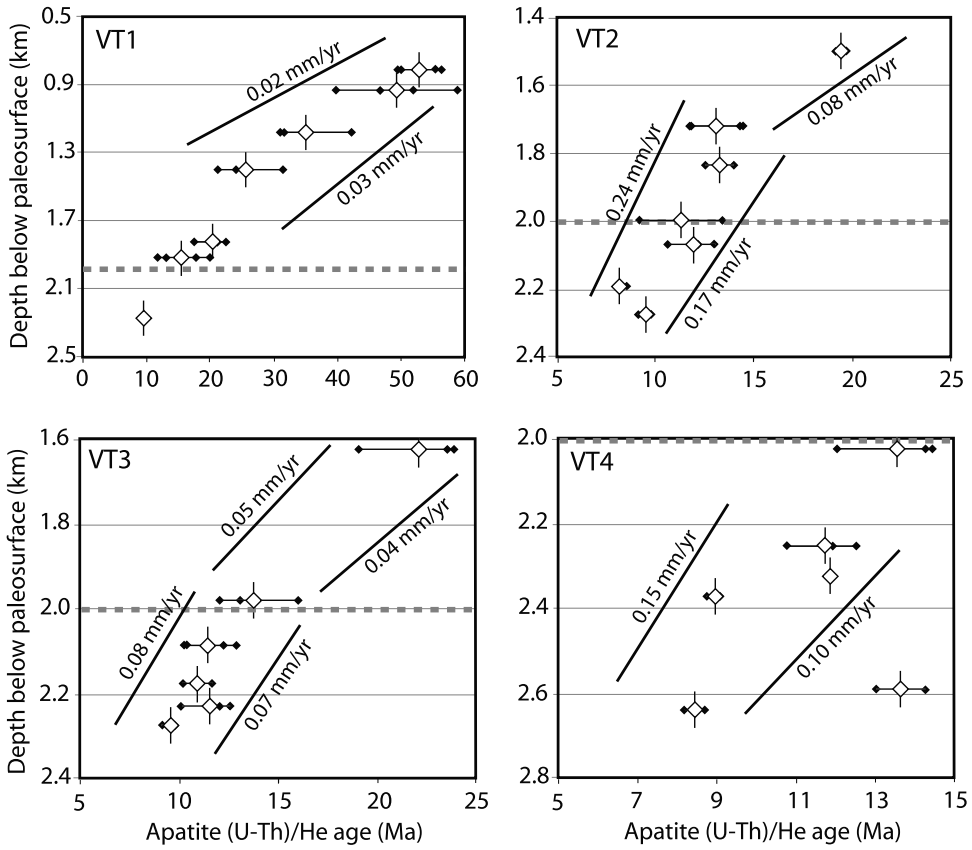

Figure 5. Valley wall transects of apatite (U-Th)/He data. In each plot, the dashed gray line marks the 2 km depth below the paleosurface. Black diamonds show individual crystal ages, and white diamonds show the mean age for each sample. Uncertainty in the depth plotted is estimated at ±100 m. Transect locations shown in Figure 1.

farther up the main valley (05TS02), and one sample we believe was from a landslide block (05TS12, circled in Figure 4). An additional valley wall transect not plotted in Figure 4 was collected from a side valley (VT0 in Figure 1, samples 05TS12, 06TS01, 06TS02, and 06TS03) and showed anomalously young ages compared to the trends shown in the other transects. Preserved remnants of a 2.01 ± 0.03 Ma (Table 2, sample 07TS12, first reported by *Schildgen et al.* [2009]) ignimbrite perched on the south side of the valley at similar elevations as the samples from VT0 suggest the ignimbrite may have partially reset apatite (U-Th)/He ages in that transect. The upper three samples from transect VT2 (06TS09, 06TS10, and 06TS11) also show ages that are significantly younger than the trend shown on the regional compilation (Figure 5). Although both transects could have been affected by the ignimbrite, another possibility is that the tributary valleys from which these samples were collected were incised well after the trunk stream. Initial analyses of the data showed that no combination of parameters could accurately predict the age of the entire suite of samples if these were included. Because our topographic evolution scenarios do not account for potential variations in trunk stream and tributary incision timing, and because of the possibility of reheating by the 2 Ma ignimbrite, we chose to exclude these samples from further analysis.

4. Thermal Model of Thermochronometer Cooling Ages

4.1. General Description

[18] We use a modified version of the finite element thermal model Pecube [*Braun*, 2002a, 2002b, 2003] and a coupled age prediction model to conduct landscape evolution scenarios and predict thermochronometer ages incorporating the thermal effects of isotherm deflection due to topography, transient thermal effects due to relief change, lateral variation in geothermal gradients due to plate subduction, and local elevation-dependent variations in surface temperature. The model solves the transient three-dimensional advection-diffusion equation with internal radiogenic heat production. The thermal field within the model domain is controlled by internal heat production, diffusion of heat from a fixed-temperature basal boundary, and advection of heat to the surface resulting from surface denudation. Primary model outputs include a three-dimensional transient temperature field, and predicted apatite and zircon (U-Th)/He cooling ages across the surface topography. We modified the program to allow lateral variations in basal temperature (T_b) across the

Table 3. Thermal and Material Properties for Model Simulations

Parameter or Constant	Range	Reference[a]	Value/Range Used
Thermal conductivity (W/mK)			
Gneiss	1.7–8.0 (3.1)	4, 6, 12	2.8
Granite	2.0–9.0 (3.2)	4, 6, 12	2.8
Granodiorite	3.3–3.8; 2.6–2.9	16, 1	2.8
Quartzite	2.1–4.1 (3.1)	4	2.8
Heat production (uW/m^3)			
Granite	2.45–2.5	3, 13	0.8
Granodiorite	1.5	13	0.8
Diorite	1.08–1.10	3, 13	0.8
Crustal average	0.8–0.9	13, 14	0.8
Specific heat capacity (J/kgK)			
Gneiss	770–979	2, 10, 11	
Granite	600–1172	8, 9	
Granodiorite	650–1046	1, 8, 9	800
Diorite	1140	2	
Quartzite	699–1013	2, 7	
Thermal diffusivity (km^2/myr)			
Granodiorite	32.8–39.7	1	40
Typical, based on above values	40.1	1	40
Basal temperature near trench (°C)	0–100	14	0
Basal temperature gradient (°C/km)	ca. 5–15	14	7–14
Density (kg/m^3)			
Gneiss	2700	2, 10, 11	
Granite	2620–2670	8, 9, 13	
Granodiorite	2700–2840	1, 8, 9	2750
Diorite	2820–2870	2, 13	
Quartzite	2640	2, 7	
Lapse Rate (°C/km)	6.5	19	6.5
Heat flow (mW/m^2)			
Central Peru offshore	30–45	15, 14	n/a
South Peru forearc	32–60	5, 14	n/a
Peruvian arc and Altiplano	50–180	5, 16, 17, 18	n/a
Geothermal gradients (°C/km)			
Peru forearc	12–21	5	n/a

[a]1, *Arndt et al.* [1997]; 2, *Èermák and Rybach* [1982]; 3, *Haenel et al.* [1988]; 4, *Hamza et al.* [2005]; 5, *Henry and Pollack* [1988]; 6, *Ehlers* [2005]; 7, *Kappelmeyer and Haenel* [1974]; 8, *Mel'nikova et al.* [1975]; 9, *Moiseenko et al.* [1970]; 10, *Schön* [1996]; 11, *Dortman* [1976]; 12, *Vorsteen and Schellschmidt* [2003]; 13, *Pollack* [1982]; 14, *Springer* [1999]; 15, *Yamano and Uyeda* [1990]; 16, *Springer and Förster* [1998]; 17, *Henry* [1981]; 18, *Uyeda et al.* [1980]; 19, *Klein et al.* [1999].

domain to more accurately simulate the thermal field above a subduction zone. The cooling histories of rocks exposed at the surface today were tracked through time and used to predict apatite and zircon (U-Th)/He ages as a function of cooling history [*Ehlers*, 2005] and grain size [*Farley*, 2000]. Helium ages are predicted using the diffusion kinetics in zircon from *Reiners et al.* [2004] and in apatite from *Farley* [2000].

4.2. Model Parameters and Boundary and Initial Conditions

[19] Model parameters include the domain size and resolution, material properties, background exhumation rate (which sets the rate at which material is advected vertically through the model domain), boundary conditions, and the style of landscape evolution. The values or ranges of model parameters used in this study are summarized in Table 3. Material properties such as heat production and diffusivity are modeled as spatially invariant and were not changed in different simulations. Values were chosen based on observed lithologies and reported material properties for those lithologies. Initial sensitivity tests revealed that variations within the reported range generally yielded insignificant effects on final results, so we did not test them further. The simulated region in this work is centered on Ocoña canyon in a N–S orientation, with dimensions of 215 × 100 km across the surface and 60 km deep (Figure 6a). This domain size is large enough to prevent boundary effects from biasing heat flow and predicted ages. The orientation of our simulation area as well as our sample transect (generally N–S) is subparallel to the slab dip, which is approximately NE–SW [*Cahill and Isacks*, 1992]. This should not have a significant effect on our results, as the only anticipated difference is a greater spatial distance between maximum and minimum values in temperature and heat flow across our sample transect compared to a transect parallel to the slab dip.

[20] We consider free parameters to be the variables that changed for the different simulations. These include initial basal temperature at the southern edge of the model (T_0), lateral basal temperature (T_b) gradient, surface relief prior to the latest phase of incision, background exhumation rate, and onset and end times of canyon incision.

[21] Previous 2-D thermal modeling and surface heat flow analysis by *Springer* [1999] (Figure 6b) provided guidelines for our basal boundary condition. *Springer*'s [1999] model suggests that basal temperature (T_b) at

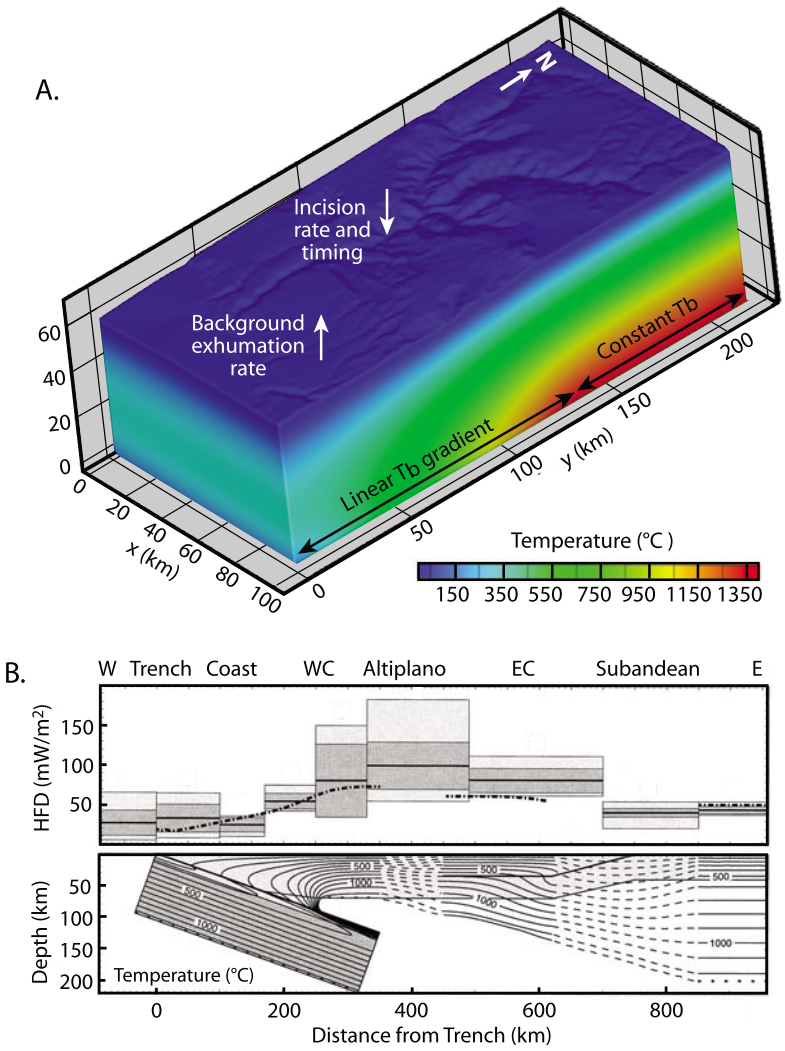

Figure 6. (a) Model setup and description. Model consists of a three-dimensional finite element grid that tracks the cooling history of each cell through time and allows for evolving surface topography. Surface temperature is described by a temperature at sea level (25°C) and a lapse rate of 6.5°C/km. The surface experiences a uniform background exhumation rate. Topography changes through time by warping from one DEM input file to another (see text for details). Heat production rate and thermal diffusivity are uniform and specified within the crust (details in Table 3). Temperature at the base of the model domain is defined by a constant value at the base of the model beneath the coast (T_0) and a linear lateral basal temperature (T_b) gradient that increases to a maximum of 1400°C, beyond which basal temperature remains constant at 1400°C. This provides an approximation of the thermal structure of a subduction zone similar to that modeled in northern Chile by *Springer* [1999]. The position of maximum temperature is controlled by both T_0 and the lateral T_b gradient. (b) Model-calculated temperature field along a W–E profile, the resulting heat flow pattern (dashed line), and measured heat flow compiled between 15 and 30°S showing mean absolute deviation range (dark gray shaded) between minimum and maximum values (shaded), simplified from *Springer* [1999] with permission from Elsevier. WC, Western Cordillera; EC, Eastern Cordillera.

~60 km depth near the coast should be approximately 200°C and should increase to a maximum temperature of ~1400°C beneath the volcanic arc. For our model simulations, we explored setting T_b between 110 and 400°C at the base of the model beneath the coast (referred to as the T_0 value) and imposed a linear temperature increase between 10.45 and 15.05°C/km, which placed 1400°C temperatures between ~66 and 123 km inland from the coast. Farther inland, T_b remained at a constant value of 1400°C. Despite the absence of a subducting slab in our model, the temperature field throughout the model domain above ~50 km depth is very similar to that modeled by *Springer* [1999] (Figure 6).

[22] The top (topographic) boundary condition used a temperature of 25°C at sea level [*Klein et al.*, 1999] and decreased with elevation following a lapse rate of 6.5°C/km. Surface temperatures changed during the simulation if the

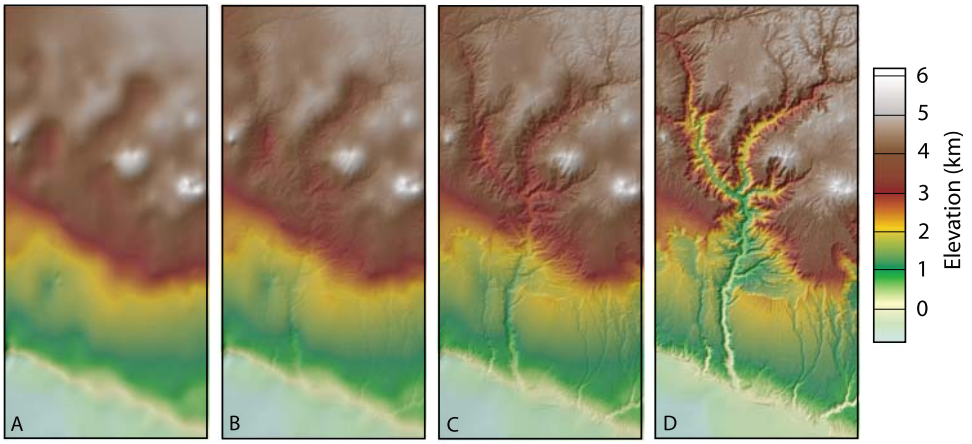

Figure 7. Examples of the digital elevation models (DEMs) used as input topographies for model simulations. All simulations started with the (a) spline topography and ended with the (d) modern-day topography. Additional simulations run to test the effects of different canyon depths prior to the latest phase of incision used additional input topographies such as the middle two frames, which show similar elevations of the canyon interfluves but only a fraction of the modern-day relief on the canyon. DEM in Figure 7b was created by multiplying the modern topography DEM by 0.1 and adding this to the spline topography multiplied by 0.9. This results in a DEM with 10% of the modern canyon relief but no significant change to interfluves elevations. DEM in Figure 7c was constructed by a similar method, resulting in 30% of the modern canyon relief.

topography evolved to new elevations. Imposed background exhumation rates explored in this study ranged from 0.01 to 0.06 mm/yr [*Schildgen et al.*, 2007; *Kober et al.*, 2007]. A zero flux boundary condition was used on the sides of the model. The initial condition used in each simulation was the steady state solution for the applied boundary conditions, background exhumation rate, and material properties. Specific values of material properties used are given in Table 3.

4.3. Topographic Evolution

[23] Surface topography in the model is defined explicitly by input synthetic and modern-day digital elevation models (DEMs), and not determined by hillslope and river erosion processes. Landscape evolution is simulated by a linear morphing function from one DEM to another. Our topographic evolution involves simultaneous onset of incision at all points along the canyon, with more rapid incision occurring in regions that today are the deepest. This scenario ignores potential waves of incision that may result from migrating knickpoints, but is probably reasonable for an area that likely experienced differential uplift from the coast to the interior across a broad monocline [*Schildgen et al.*, 2009], which would have led to simultaneous steepening along most of the river profile.

[24] Two end-member topographic scenarios considered in this study include steady state topography and canyon incision. For steady state simulations, the canyon and present-day topography existed prior to and throughout the simulation (Figure 7d). These simulations explored the simplest case of steady state topography and a spatially and temporally constant exhumation rate. The canyon incision simulations comprised a series of simulations that varied the timing and magnitude of incision into a smooth surface that ramps from the coast up to the plateau. Topography was morphed from the spline DEM (discussed below) (Figure 7a) to intermediate-relief topography (e.g., Figures 7b and 7c) and then to the final, high-relief modern topography (Figure 7d). The timing and rate of incision between individual steps shown in Figure 7 were treated as free parameters and are discussed later.

[25] The 250 m resolution DEMs used in the simulations were resampled from 30 m resolution DEMs created from Advanced Spaceborne Thermal Emission and Reflection Radiometer (ASTER) imagery (Figure 7d). Initial topography prior to canyon incision (Figure 7a) was generated by selecting points on the preserved paleosurface on canyon interfluves and using a spline (piecewise polynomial) interpolation to smooth out canyon relief, but still retain the general morphology of ramping from the coast up toward the plateau (for details see *Schildgen et al.* [2007]). We refer to this as the ''spline DEM.'' In order to explore the effect of different paleocanyon depths on predicted thermochronometer age patterns, we created a series of synthetic DEMs (e.g., Figures 7b and 7c) that maintained nearly unchanging elevations for canyon interfluves, but approximated the canyon morphology for earlier stages in the incision history. These DEMs were generated by first multiplying all values in the modern-day DEM by a small fraction (for instance, 0.2), which reduced both total relief and absolute elevation of all points. This layer was then added to a complementary fraction of the spline DEM (for instance, 0.8) in order to create a DEM that maintained the absolute elevation of points on the canyon interfluves while reducing canyon relief. These intermediate layers allowed us to test the effect of differing canyon depths prior to the latest phase of incision.

4.4. Evaluation of Model Results

[26] We conducted 275 simulations to explore a range of incision histories and other model free parameters. Each simulation was assessed using two metrics to evaluate if the model produced an acceptable fit to geologic observations, including (1) minimization of the chi-square misfit between

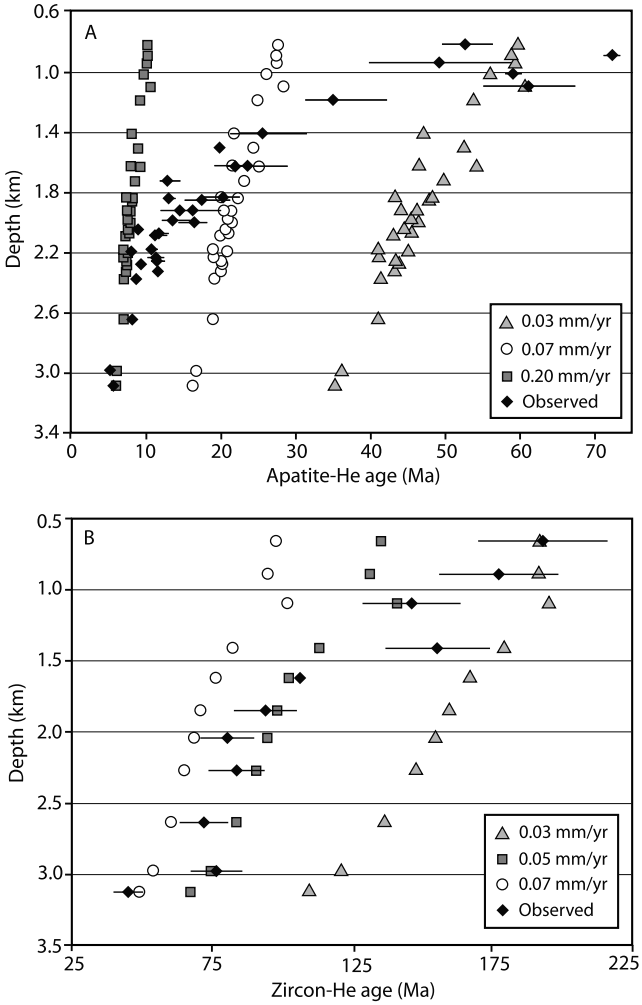

Figure 8. Model predictions for steady state topographic evolution scenarios compared to observed ages (black diamonds with 2σ error bars). Basal temperature beneath the coastline (T_0) was set to 180°C, and lateral basal temperature (T_b) gradient was set to 13.9°C/km. Results plotted show the effect of varying background exhumation rate on predicted (a) apatite and (b) zircon (U-Th)/He ages.

predicted and observed apatite and zircon (U-Th)/He ages, and (2) a test if the range of predicted surface heat flow values fell within the observed range. Regional heat flow determinations [*Henry and Pollack*, 1988; *Hamza and Munoz*, 1996; *Springer and Förster*, 1998; *Hamza et al.*, 2005] show the modern-day range of geothermal gradients in the region as well as the magnitude of lateral changes from near the coast toward the volcanic arc. We used a chi-square goodness of fit test to quantify the quality of fit between our observed thermochronometer ages and model-predicted ages, and to determine best fit scenarios. The chi-square misfit is calculated as the sum of the squared differences between observed thermochronologic ages and expected model ages divided by the variance of the observed ages (equation (1)). The variance does not include the analytical error, as this is generally small compared to the range of observed ages.

$$\chi^2 = \sum_{i=1}^{n} \frac{(\mathrm{obs}_i - \mathrm{exp}_i)^2}{\sigma_i^2} \quad (1)$$

[27] For each sample, the standard deviation (σ) was calculated from the range of individual crystal ages. For samples that consisted of only one or two analyzed crystals, we assumed that the standard deviation was equal to 15% of the mean age, as this was the average value for the multi-crystal analyses. We compared the chi-square misfit to a critical value that is associated with a 95% confidence level. This is determined by comparison with a chi-square distribution, typically recorded in tables such as in the work of *Pearson and Hartley* [1966]. The critical value is a function of the number of samples to which model results are compared, as well as the number of free parameters in the model. If the chi-square sum is below the critical value, then the model predictions give a good match to the observed ages at the given confidence level. This is a reasonable statistic to assess low-temperature thermochronometry data, where ages generally show poorer reproducibility with increasing age, but the magnitude of error on any particular mean age is difficult to assess (see discussion in the work of *Ehlers* [2005]). We assume that chi-square values that fall below the critical value associated with a 95% confidence interval result in model predictions that are predominantly within error of sample mean ages.

5. Model Results

[28] We conducted 275 model simulations over a wide range of parameter space to find best fit scenarios and to discern the sensitivity of predicted ages to different exhumation histories. In the following sections we discuss the quality of fit between model predictions and both apatite and zircon data for simulations that explored background denudation rates and different gradients in basal temperature. However, for simulations that specifically explored details of the canyon incision process, we only discuss the quality of fit for apatite data. The zircon data showed no variation in simulations that only explored details of canyon evolution because their greater closure depth prevents them from recording the near-surface thermal effects of canyon incision (see discussion in the work of *Schildgen et al.* [2007]).

5.1. A Test of Steady State Topography

[29] Steady state topographic simulations started and finished with the modern-day topography. We ran 40 simulations with T_0 set to 180°C at the base of the model beneath the coast, T_b increasing at a rate of 13.9°C/km toward the arc, and a range of denudation rates from 0.01 to 0.22 mm/yr. Denudation rates were set constant over the entire simulation duration from 250 Ma to today. All other parameters such as material properties are presented in Table 3.

[30] Model results indicate that the range in ages predicted for a constant exhumation rate is relatively small, though it increases with slower rates. For example, an exhumation rate of 0.20 mm/yr yields apatite ages from ~7 to 9 Ma, a 0.07 mm/yr rate produces a range from ~16 to 25 Ma, and a 0.03 mm/yr rate results in ages from ~35 to 60 Ma (Figure 8a). Results show that a single exhumation rate cannot produce the age variability observed in the apatite data.

[31] Steady state model simulations produce better matches to portions of the zircon (U-Th)/He data, but poor

fits to the whole set. An exhumation rate of 0.05 mm/yr shows good fits between predicted and observed ages that are less than 125 Ma, but a slower exhumation rate is needed to match older samples (Figure 8b). In summary, none of the simulations that assumed steady state topography produce a statistically acceptable fit (within a 95% confidence interval) for the apatite and zircon data.

5.2. Canyon Incision and Transient Topography

[32] To explore the effect of incision timing and magnitude on predicted ages, we started 235 simulations with the spline DEM (Figure 7a) and investigated the influence of canyon incision onset between 7 and 12 Ma, incision completion between 2 and 6 Ma, and variations in early canyon maximum depths ranging from 200 to 1120 m, corresponding to 6 to 35% of the modern canyon relief. The following sections describe these topographic scenarios in greater detail and the additional parameters that affect model results.

5.2.1. Background Exhumation and Basal Temperature

[33] We explored the relationship between lateral T_b gradient and background exhumation rates to determine a reasonable range of values for these parameters through 50 model simulations. All other parameters were held constant and values used are summarized in Table 3. For the following simulations, we set the initial topography to be the spline DEM (Figure 7a), set background exhumation rate to be constant over the 225 million year duration of the run, and morphed topography from the spline DEM to the modern-day topography (i.e., incised the canyon) between 10 and 2 Ma.

[34] Model results show that background denudation rate and lateral temperature gradient have a strong effect on predicted apatite (U-Th)/He ages. When denudation rate is set to 0.012 mm/yr and T_0 is 200°C, a lateral T_b gradient of 15.05°C/km produces best fits to the data (Figures 9a and 9b). Chi-square misfit values calculated for expected and observed apatite ages over a range of lateral T_b gradients and denudation rates are shown in a contour plot in Figure 9c. These illustrate that increasing lateral T_b gradients require lower exhumation rates to derive best matches to the data, with the best results from exhumation rates ranging from ~0.011 to 0.015 mm/yr and lateral T_b gradients from ~13 to 15°C/km. These simulations produced a range of surface heat flows from near the coast to just south of the volcanic arc of ~40 to 55 mW/m^2 for a lateral T_b gradient of 10.45°C/km and ~50 to 65 mW/m^2 for a gradient of 15.05°C/km. The whole range of tested lateral gradients are reasonable considering the range of modern-day measurements of ~30 to 60 mW/m^2 from coastal to inland regions of the forearc.

[35] The observed zircon (U-Th)/He data are not well predicted by uniform background denudation rates (Figures 9d–9f). On both age versus depth (Figure 9d) and distance from coast versus age (Figure 9e) plots where the lateral T_b gradient is 13.9°C/km, denudation rates of 0.045 mm/yr show a good match to zircon ages less than 125 Ma or closer than 45 km to the coast. Observed ages greater than 125 Ma and farther inland are better matched by a 0.035 mm/yr denudation rate. However, simulated heat flow values from ~60 to 80 mW/m^2 across the forearc region are higher than modern values. Furthermore, even the lowest chi-square misfit values far exceed the critical value of 12.6 over the entire parameter space (12 samples with 6 free parameters in the model), suggesting that a uniform background denudation rate is not appropriate for explaining the zircon data. Instead, spatial and/or temporal variations are likely. Alternatively, the data may reflect changing thermal conditions in the crust, possibly related to plutonism. Because testing these different possibilities would require a more extensive zircon-He data set than what is currently available, and because the details of exhumation history prior to ~40 Ma have insignificant effects on regional interpretations of the incision history, we do not further explore the details of early (pre-40 Ma) exhumation and thermal evolution.

5.2.2. Incision Timing

[36] Although onset of the latest phase of incision should be close to the observed break in slope in the apatite data, imprecision in the data, rounding of the break between older and younger ages due to effects of the helium partial retention zone, and lag in thermal response to incision make identification of an onset time difficult. Estimating the timing of incision completion is even more difficult because the base of the rapidly cooled zone is not exposed, hence must be inferred from modeling or from other geological constraints. *Schildgen et al.* [2007] estimated incision completion to be no later than ~2.3 Ma, based on the age of a volcanic flow perched 100 m above the present valley floor. A more precise estimate is no later than 2.21 ± 0.02 Ma, based on a new $^{40}Ar/^{39}Ar$ age of a volcanic flow collected from the present valley floor (Figure 2 and Table 2). Unfortunately these flows only provide broad constraints on incision rates, as each flow only tells the minimum time that incision reached the depth of the observed base of the flow, and the deepest part of the flow may have been removed due to erosion.

[37] Given these general guidelines, we tested a range of onset times between 7 and 12 Ma, and completion times between 2 and 6 Ma. There was no change in topography after the completion time, but background exhumation (advection of material to the surface) continued to 0 Ma. In the simulations presented, we show best estimates for incision onset and completion time assuming a range of T_0 (temperature at base of model beneath the coastline) and lateral T_b gradient combinations. For any given combination, the suite of chi-square values produced from different onset and completion times are sensitive to changes in exhumation rate on the order of 0.001 mm/yr. Thus, we first identified the exhumation rate that produces minimum chi-square values, and show how best fits for incision timing are affected with the different combinations. All other parameters were held constant (see Table 3).

[38] Results from 125 simulations illustrate the effects of changing T_0 and the lateral T_b gradient. In general, minimum chi-square values cover a shorter range of onset times than completion times, meaning that the former can be determined with greater precision. Because there are 24 total samples included in the analysis and 6 free parameters, the critical value associated with a 95% confidence interval when comparing all model results is 28.9. Lowest chi-square values are produced over the widest range of onset and completion times when T_0 is set to between 180°C and 200°C with a lateral T_b gradient of 13.9°C/km to 15.05°C/km (Figure 10). Over the whole range of explored parameter space, chi-square sums that are below the 95% confidence interval

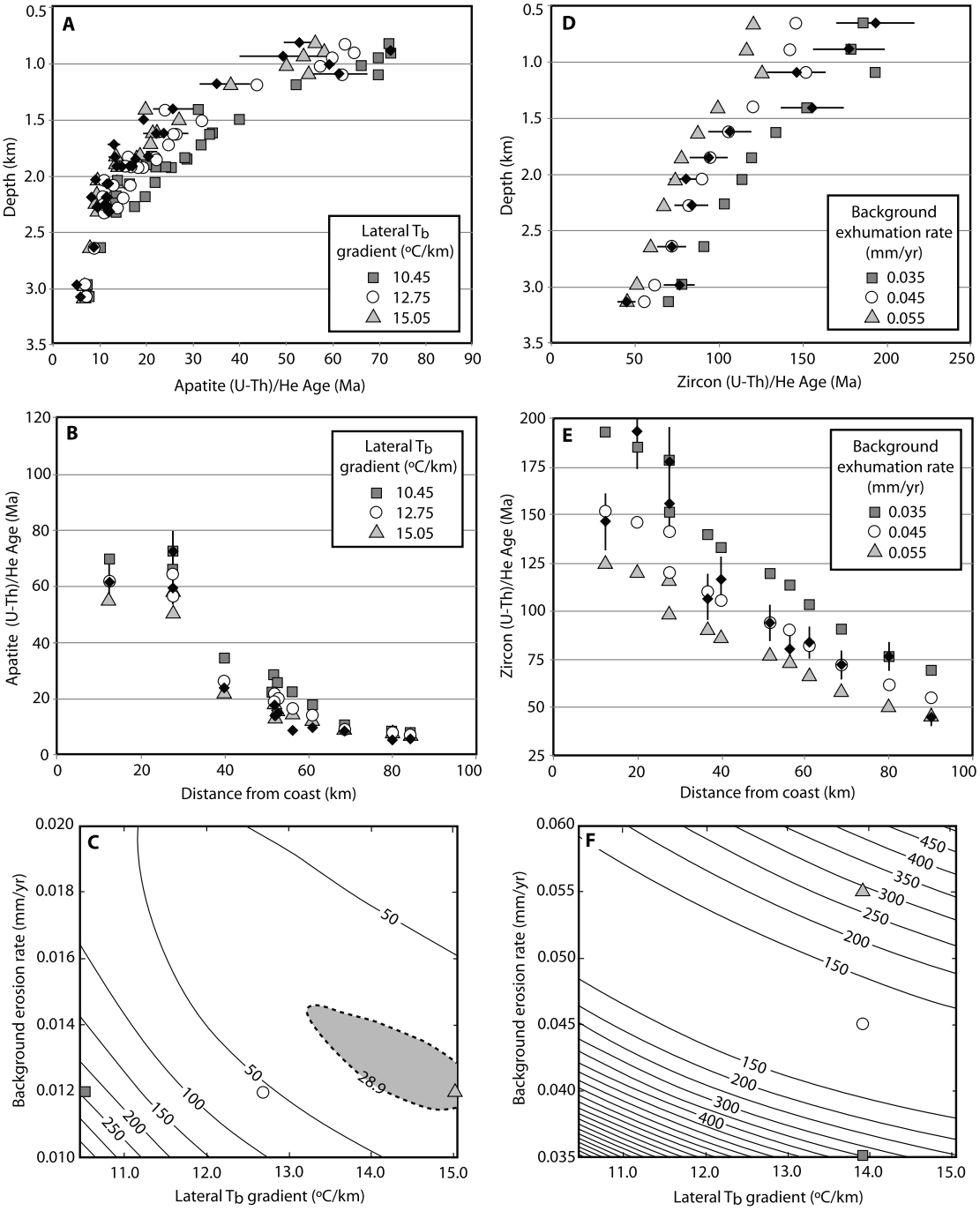

Figure 9. Model results for simulations exploring the effects of background exhumation rate and lateral basal temperature (T_b) gradient on predicted thermochronometer ages, and comparisons with observed ages. Figures 9a–9c show comparisons between model-predicted ages and observed (U-Th)/He ages for apatite samples. Parameters held constant include incision onset time (10 Ma), incision completion time (2 Ma), basal temperature beneath the coast (T_0 = 180°C), background exhumation rate (0.012 mm/yr), and the topographic evolution scenario is from the spline DEM to the modern topography. (a) Results on a depth (beneath paleosurface) versus age graph. (b) Results on a distance from coast versus age graph. (c) Contour plot of chi-square misfit values between predicted and observed ages over a wide range of lateral T_b gradients and background erosion rates, with the shaded region indicating values less than the critical value of 28.9. Contour intervals are labeled with chi-square values. The square, circle, and triangle in Figure 9c show the exhumation rate and lateral T_b gradient values illustrated in Figures 9a and 9b. (d and e) Comparison of predicted and observed (U-Th)/He ages for zircon for a given lateral basal temperature (T_b) gradient (13.9°C/km) and a range of background exhumation rates; (f) contour plot of chi-square misfit values over a range of lateral (T_b) gradients and exhumation rates. The square, circle, and triangle in Figure 9f show the exhumation rate and lateral T_b gradient values illustrated in Figures 9d and 9e.

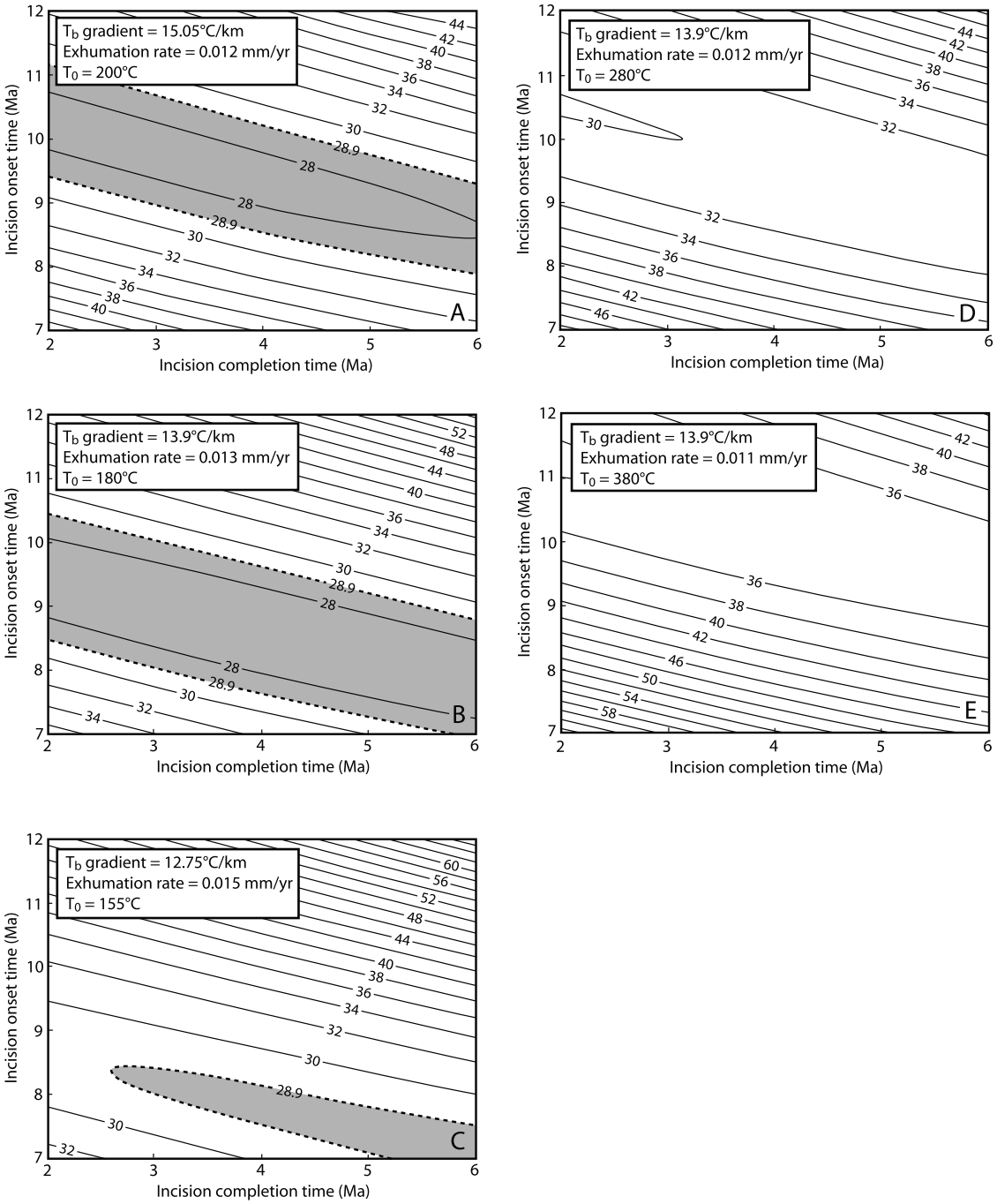

Figure 10. Contour plots of chi-square values showing model-predicted incision timing compared to the whole set of apatite samples for various combinations of T_0, lateral T_b gradient, and best fit background exhumation rate. The critical value associated with a 95% confidence interval for the 24 samples and 6 free parameters is 28.9. This value is marked by a dashed gray contour line and values that fall below are shaded in gray.

(dotted lines) fall within the range of ~7 to 11 Ma for incision onset time. Minimum values occur at completion times covering the whole tested range from 2 to 6 Ma, with earlier completion times associated with later onset times. Differences in the quality of fit are also illustrated on an age-depth plot for three simulations (Figure 11).

5.2.3. Incision Magnitude

[39] Simulations to test the effects of different initial canyon depths proceeded from the spline DEM to an intermediate layer, then from the intermediate layer to the modern topography starting at 9 Ma, and completion of canyon incision at 2 Ma. The spline layer itself contributes initial relief of approximately 200 m in the deepest reaches of the canyon. We tested two different start times for the generation of higher magnitudes of initial canyon relief: 50 to 30 Ma, the estimated time of Lower Moquegua Formation red bed deposition in southern Peru, and 30 Ma to 14 Ma, the time of Upper Moquegua sand/conglomerate deposition [*Sempere et*

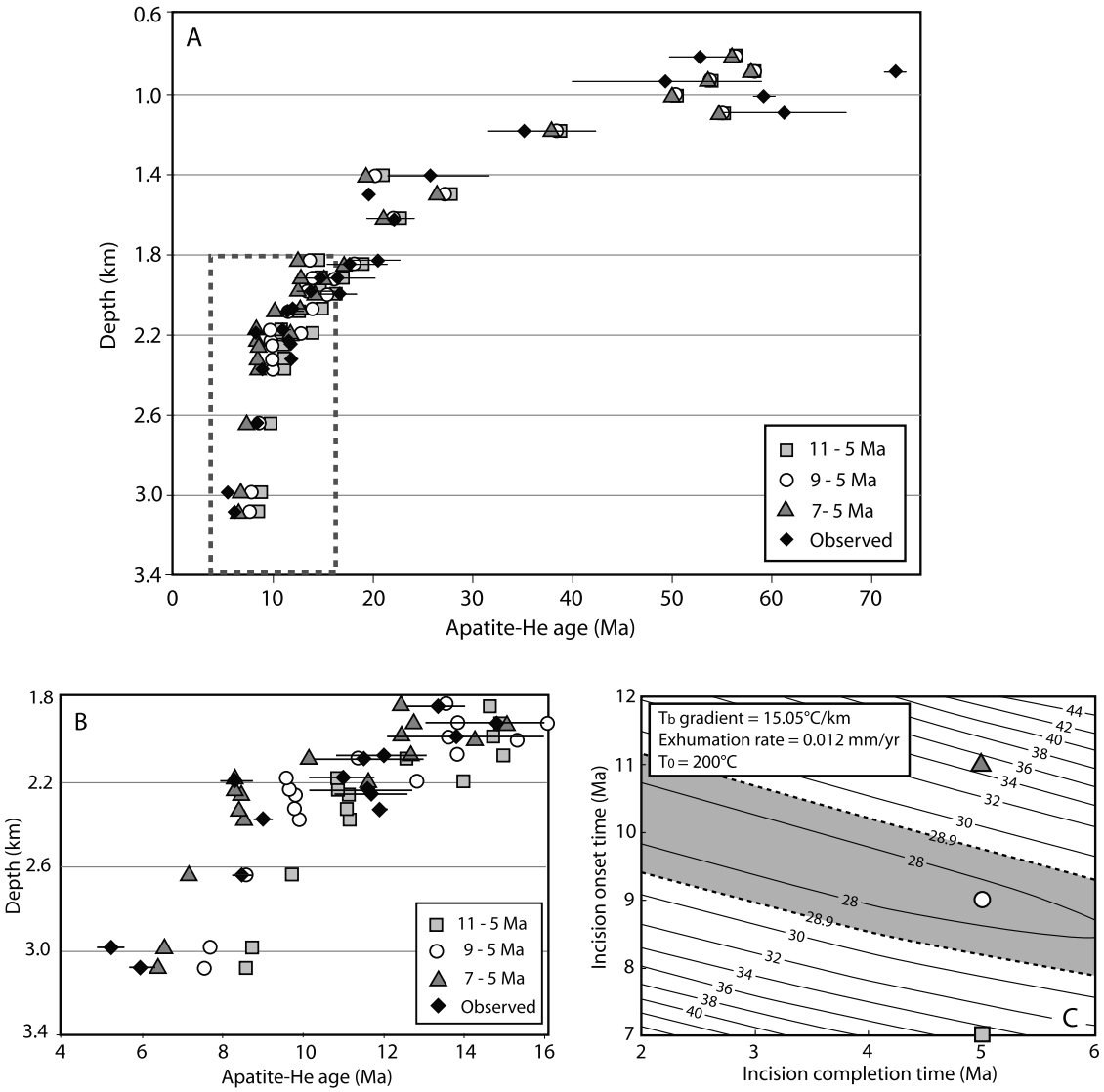

Figure 11. Age-depth plots of observed and simulated data exploring the timing of canyon incision. (a) Results of simulations and observations where basal temperature beneath the coast (T_0) was set at 200°C, lateral basal temperature (T_b) gradient was set to 15.05°C/km, and background exhumation rate was set to 0.012 mm/yr. The time range listed in the legend refers to the time span of canyon incision. (b) Zoom in to the set of data less than 16 Ma. (c) Contour plot of chi-square values calculated for the whole sample set, with an associated critical value of 28.9 at a 95% confidence level. The region shaded in gray shows the area of parameter space that falls below that value. The square, circle, and triangle in Figure 11c illustrate the position where the results plotted in Figure 11a lie in parameter space.

al., 2004; *Roperch et al.*, 2006]. The former may represent the development of early inland topography in the region, while the latter may represent first generation of significant topography. Initial canyon relief tested included 10%, 20%, 25%, 30%, and 35% of the modern canyon relief, which correspond to approximately 320, 640, 800, 960, and 1120 m depths in the deepest reaches of the canyon. Background exhumation rates were set at 0.013 mm/yr and the range of early canyon depths was tested against a range of lateral T_b gradients from 10.45 to 15.05°C/km.

[40] Results from 60 simulations show significant effects of initial canyon relief on predicted ages. For initial incision occurring from either 50 to 30 Ma or from 30 to 14 Ma, model results are generally much worse than those predicted with no initial incision (Figure 12).

6. Discussion

6.1. Valley Wall and Valley Bottom Transects

[41] Final outputs of the model include a prediction of thermochronometer ages at every point on the landscape surface. From this surface of predicted ages, we extracted profiles of predicted ages along the valley bottom and sidewalls. This allows for a more general assessment of the differences between valley bottom and valley wall transects. Extracted profiles show that despite an overlap in the rapidly

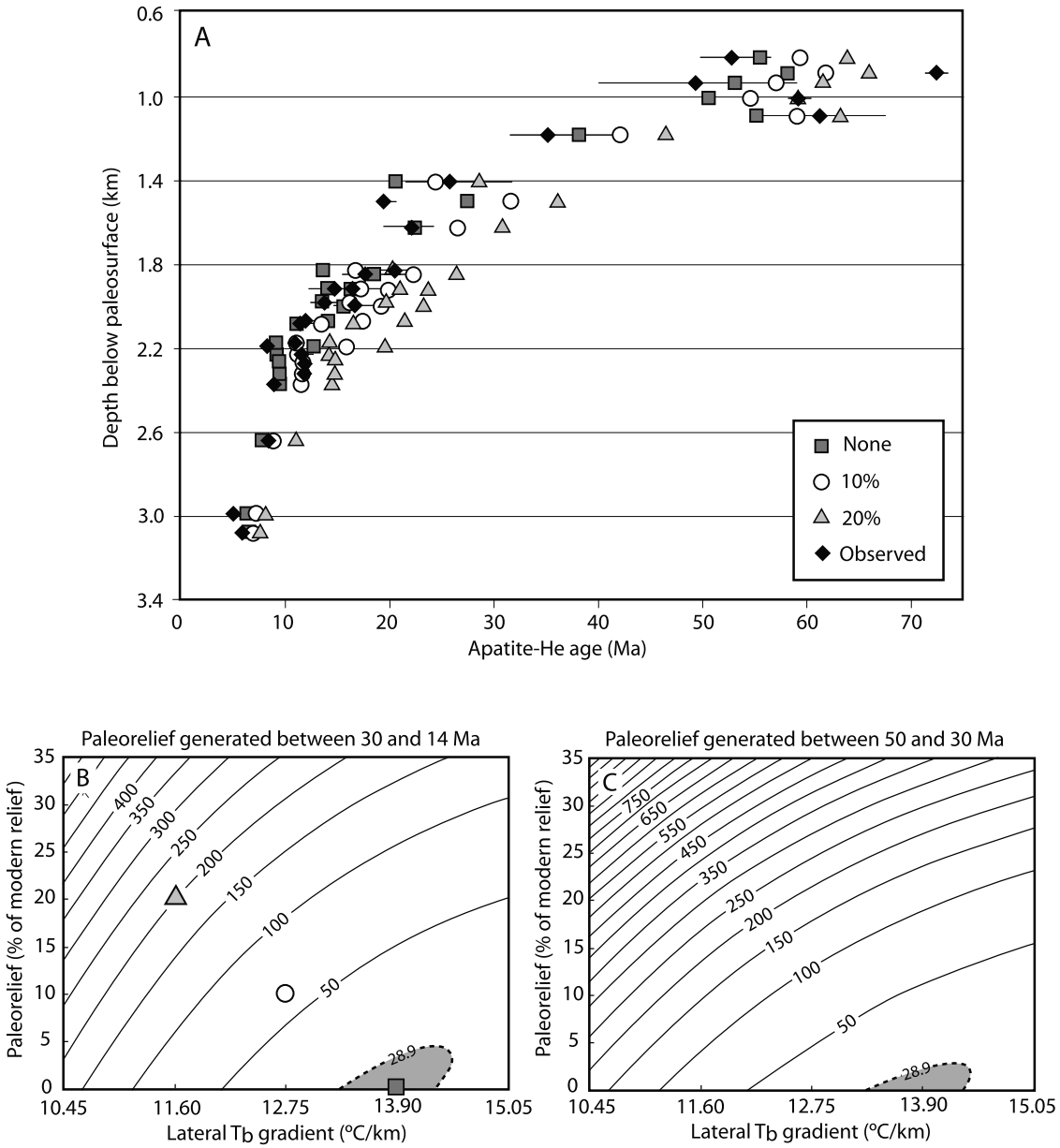

Figure 12. Model-predicted ages of various magnitudes of early canyon relief compared to observed apatite data. Percent relief refers to the percentage of modern canyon relief that existed prior to the latest phase of incision. (a) Results of simulations and observed data on an age-depth plot for initial canyon relief generated between 30 and 14 Ma and final incision between 9 and 2 Ma. Background exhumation rates and lateral T_b gradients for the plotted results are shown in Figure 12b (square, circle, and triangle). (b and c) Contour plots of chi-square misfit values, for early incision generated between 30 and 14 Ma (Figure 12b) and between 50 and 30 Ma (Figure 12c). Chi-square values were calculated using the whole sample set with an associated critical value of 28.9 at a 95% confidence level.

cooled portion of both profiles, the valley bottom transect shows a more gentle slope in the older, slowly cooled region (solid versus dashed line in Figure 13). The model-predicted differences between valley wall and valley bottom profiles closely mimic the differences observed in measured ages from valley wall and valley bottom transects (black versus white diamonds in Figure 13). These differences are a direct consequence of the change in geothermal gradient along the forearc-traversing valley bottom transect. Compared to the valley wall transect, which samples across a nearly uniform geothermal gradient, the wider range in gradients across the valley bottom transect leads to a wider distribution of ages, and a lower slope on a depth versus age plot (Figure 13a). This decreased slope is likely to be a consistent bias in transects that sample across a wide region with changing thermal properties, even when the data are plotted against depth to correct for long-wavelength topographic effects on the shape of the closure temperature isotherm.

[42] In addition to this bias inherent to the type of sample transect, both profiles exhibit a curved transition between

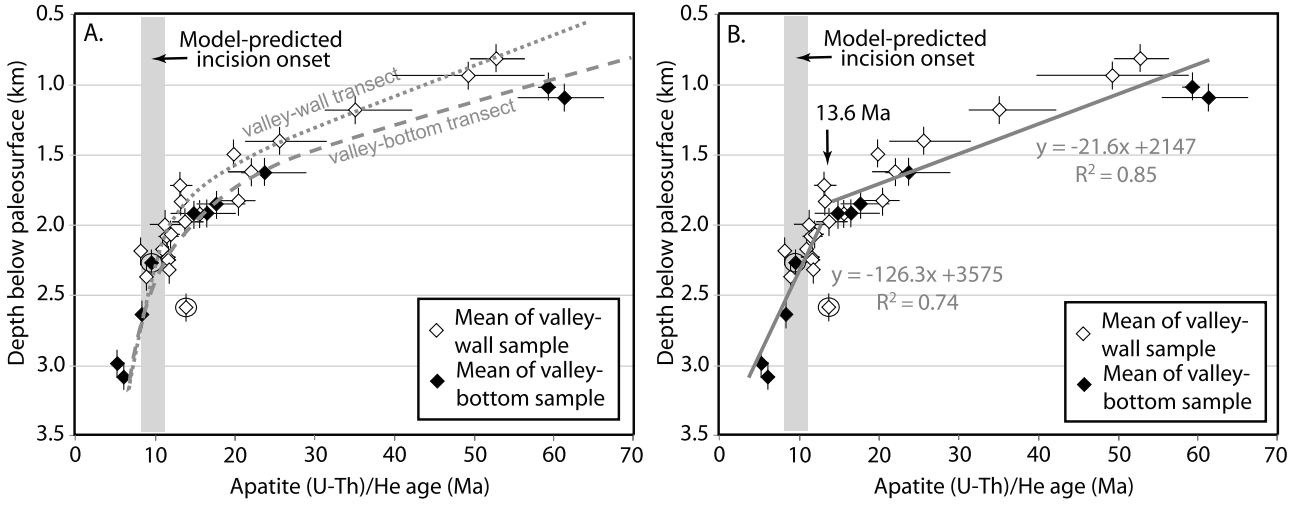

Figure 13. (a) Valley wall and valley bottom transects extracted from model results compared to observed data. Model valley wall transect (dotted gray line) was extracted from the west side of the valley near sample 05TS37 (Figure 1). Model valley bottom transect (dashed gray line) was extracted from a line along the valley bottom starting at the coast and moving inland as far as the confluence of two main valleys ~10 km northwest of sample 05TS37. Model transects plotted are from a simulation that included incision between 10 and 2 Ma, T_0 of 180°C, a lateral T_b gradient of 13.9°C/km, and a background exhumation of 0.013 mm/yr, though the general pattern shown here (with a more gentle slope in the slowly cooled region of the valley bottom data) was consistent across all model simulations and reflects the regional heat flow gradient (Figure 6). Grey boxes in both plots illustrate the range of model-predicted incision onset times. (b) Linear fits (gray lines) of the upper and lower portions of the observed data (above and below 2 km depth) show an intersection at ~13.6 Ma.

the slowly and rapidly cooled regions. This is an expected resulted from the slow diffusion of He in the partial retention zone, even in the case of a sudden, major change in cooling history [e.g., *Wolf et al.*, 1998]. Both the curved shape of the transition zone and the differences between the two transects complicate visual interpretations of the data. For example, maximum curvature appears to occur at ~13 to 15 Ma in both our data and in a model simulation with incision starting at 10 Ma (Figure 13a). Similarly, linear fits through the upper and lower portions of the data intersect at ~13.6 Ma, though our modeling indicates a best fit onset of rapid cooling between ~8 to 11 Ma (Figure 13b). These examples illustrate the potential to overestimate the timing of a change in exhumation rate if thermal modeling is not incorporated into the interpretations.

6.2. Temporal and Spatial Patterns in Background Exhumation Rates

[43] Understanding temporal and spatial patterns in background exhumation rates is difficult in a region where both are likely to vary. In theory, the observed pattern of apatite ages can be predicted by a model that imposes a sharp increase in regional exhumation rates through time without any change in surface topography (i.e., steady state modern topography). However, this is unlikely, as the required increase in exhumation rates of ~0.03 mm/yr to 0.20 mm/yr would inherently require a change the surface morphology (for example, the sharp edges between canyon walls and the plateau surface are unlikely to be maintained under increasing regional exhumation rates). Also, although the climate history of southwest Peru prior to significant Andean uplift is currently not well understood, some studies suggest that precipitation (and associated regional exhumation) have decreased during the latest phase of plateau uplift. For example, climate modeling work shows that the steep western flanks of the plateau were wettest when the Altiplano was approximately half its current height [*Ehlers and Poulsen*, 2009], and paleosols in northern Chile suggest that conditions went from semiarid to hyperarid starting at 19 to 13 Ma [*Rech et al.*, 2006]. Finally, geologic relationships showing widespread clastic deposition until ~14 Ma on the uplifted regional bajada surface between Iquipi and the coast indicate little to no canyon incision at that time [*Schildgen et al.*, 2009]. These observations all support the results from our steady state topographic modeling, which showed that no simulation incorporating unchanging topography could produce a match to the observed thermochronology data. Instead, the steep gradient in apatite ages is best interpreted as localized cooling resulting from canyon incision.

[44] The role of background exhumation rates is still unclear for canyon incision scenarios. Both apatite and zircon samples near the coast show old ages with low slopes on depth-age plots (e.g., Figure 9). This shows that coastal regions have experienced low background exhumation throughout the time span recorded by both thermochronometers: ~75 to 14 Ma for apatite, and ~175 to 75 Ma for zircon. However, younger zircon samples collected from farther inland reflect faster cooling from ~75 to 40 Ma. This can be explained by several alternatives. It may reflect an earlier history of tectonic activity with accompanying faster exhumation in the interior region from ~75 to 40 Ma. This may also reflect the early establishment of the spatial gradients in precipitation and exhumation that we see today

[*Houston and Hartley*, 2003; *Bookhagen and Strecker*, 2008], where higher inland regions experience faster denudation than hyperarid coastal regions. Alternatively, faster cooling could have resulted from local perturbations to the thermal field, as would be expected from the cooling of Cretaceous age intrusive bodies (Figure 2 and Table S4). Additional data are needed to test which of these possibilities is most likely. For example, valley wall transects collected throughout the valley length from the coast toward the arc could reveal cooling rates in specific locations, and hence help discriminate between temporal and spatial changes in the cooling history of zircons.

6.3. Incision History

[45] Canyon depths prior to the latest phase of incision give information on the initial position of near-surface isotherms, which is crucial for assessing the magnitude of the latest phase of incision. In southwest Peru, depositional records suggest that the major drainages are likely to have experienced a long history of incision that started well before the most recent phase of late Cenozoic incision. Cut and fill channels up to several hundred meters deep within the ~30 to 14 Ma Upper Moquegua conglomerates [*Sempere et al.*, 2004; *Roperch et al.*, 2006] are exposed in small drainages such as the Sihuas valley, 110 km to the southeast of the Ocoña valley. This gives evidence for a drainage system prior to 14 Ma with depths of at least several hundred meters. However, deposition of thick Upper Moquegua sand/conglomerate sheets across the whole ~50 km wide forearc region would not be possible if there were one or several major canyons draining the forearc region from ~30 to 14 Ma [*Schildgen et al.*, 2009].

[46] Our model simulations that explored canyon depths prior to the latest phase of incision produced minimum chi-square values when the spline topography was used as a starting topography, which consists of ~200 m of relief in the deepest parts of the canyon. Initial incision that exceeded these depths produced chi-square values that far exceeded the 95% confidence interval, therefore we interpret forearc fluvial channels at 14 Ma to be no greater than ~200 m, although channel depths farther inland near volcanoes may have exceeded this value. Surface topography that hosted such channels must have reached elevations at least as high as 200 m above sea level. Because the total depth of the canyon today is ~3.2 km at the northern end of our sampled region (in the deepest reaches of the canyon), our interpretation of ~200 m initial canyon depths imply that the latest phase of incision (post-14 Ma) was up to ~3.0 km in magnitude, decreasing to $\leq$1 km at the coast.

6.4. Preferred Model for Canyon Evolution

[47] The geologic record provides firm evidence for topography in the Central Andes prior to 14 Ma, with fluvial conglomerate layers within the ~30 to 14 Ma Upper Moquegua Formation implying that fluvial networks existed prior to the latest phase of surface uplift [*Schildgen et al.*, 2009]. Our data are most appropriate for constraining canyon evolution after ~14 Ma, the age of the uppermost volcanic ashes that cap the Upper Moquegua sedimentary sequence and blanket the regionally extensive paleosurface. The latest phase of incision in the Ocoña region was preceded by or synchronous with spatially variable uplift that generated a ramp that is today preserved as the relatively smooth paleosurface at 1 km elevation near the coast and rises to 4 km at the plateau margin.

[48] Modeling results alone suggest that canyon incision into the newly grown topography started between 7 and 11 Ma. These results should be considered carefully, as the later onset times show poor matches with the limited number of young samples from the deepest reaches of the canyon (e.g., Figure 11c). More samples from this crucial, deeply incised region are likely to increase chi-square misfit values for simulations that show a poor match to the youngest samples, and hence may narrow the estimate for onset times. Another reason to question the late onset times is that they correspond to relatively early incision end times. For instance, simulations with a 7 Ma onset of incision have best fit end times of ~5.5 to 6 Ma (Figures 10b and 10c). However, the 5 Ma coarse, fluvial gravels stranded at elevations near 1 km close to the coast suggest that ~1 km of incision resulting from a phase of block uplift happened after 5 Ma [*Schildgen et al.*, 2009]. These uplifted coastal gravels and the 2.21 ± 0.05 Ma volcanic flow that reached the present valley bottom together suggest that incision ended sometime between ~5 and 2.2 Ma. Reconsidering the modeling results including these geologic constraints suggests that the onset of incision is between ~8 and 11 Ma.

[49] One of the main limitations to our topographic simulations is that we use prescribed DEMs to model changes in topography rather than applying erosion laws that could more accurately portray changes in landscape morphology through time. Propagation of knickpoints through a drainage system could produce incision onset times that differ by several million years between the outlet and the uppermost catchment. However, given that simultaneous onset of incision provides a statistically valid match to the whole data set, we know that either simultaneous onset of incision or rapid headward propagating incision (on the order of one million years or less over the sample transect) is consistent with the available data. For this reason, we believe that incorporating a physical model of canyon incision is unlikely to substantially change interpretations of incision timing.

6.5. Comparison to Other Estimates of Plateau Uplift

[50] Canyon incision with a magnitude up to 3.0 km starting at ~8 to 11 Ma requires contemporaneous or preceding surface uplift with at least an equal magnitude. The lag time between the start of uplift and the start of incision may be on the order of several million years or more for a detachment-limited system, but when discharge is high (such as in the trunk stream of major rivers), the lag time can be much shorter [e.g., *Whipple and Tucker*, 1999, 2002].

[51] Several sites in southern Peru and northern Chile give clues about knickpoint retreat rates, which are directly related to the lag time of the systems. In the Rio Lluta valley of northern Chile, knickpoint retreat following late Miocene surface uplift was estimated at ~10 km/Ma [*Schlunegger et al.*, 2006]. Similarly, we can infer 6 to 8 km/Ma rates of knickpoint retreat in the Sihuas valley of southern Peru, where a large knickpoint that was likely initiated on the coast at ~5 Ma is preserved on the river profile between 30 and 40 km inland [*Schildgen et al.*, 2009]. A much slower

retreat rate of ~1.6 km/Ma starting after 6.4 Ma is described in the Quebrada Tiliviche in northern Chile [*Hoke et al.*, 2007]. In contrast to these systems, the lack of any major knickpoints along the ~250 m length of the Cotahuasi-Ocoña drainage system [*Schildgen*, 2008] provides evidence that the this major drainage system has a faster knickpoint retreat rate and a shorter geomorphic lag time compared to rivers in the hyperarid catchments of northern Chile and compared to smaller rivers in southern Peru. However, additional work is needed to estimate the lag times more precisely. Despite this present uncertainty in lag time, we believe the phase of uplift documented to have started at ~10 to 11 Ma in the Altiplano interior, at the eastern margin, and in other parts of the western margin (evidence summarized in Table 1) is likely to be correlative with uplift that preceded the major pulse of incision in Ocoña canyon. Particularly compelling is the ~10 Ma initiation of long-wavelength surface deformation of foreland basin fill [*Nester*, 2008] and lake sediments [*Jordan et al.*, 2006] in northern Chile, which agree within error with our estimates for the onset of canyon incision in southwest Peru.

[52] If the data summarized in Table 1 do result from contemporaneous uplift over a ~300 to 400 km wide orogen, it was likely to have been driven by geodynamic processes that can affect the whole of an orogenic plateau, rather than isolated regions. The role of upper crustal shortening and thickening is thus less likely to have contributed to this latest phase of uplift, because such deformation is often focused on particular parts of the plateau. Processes occurring deeper within the crust or lithosphere such as regional ductile redistribution of mass through middle to lower crustal flow [e.g., *Isacks*, 1988] or changes in the subduction zone geometry [e.g., *Jordan et al.*, 1983] are more likely to affect large regions, and hence are more feasible explanations for the latest phase of plateau uplift.

7. Conclusions

[53] Three-dimensional thermal modeling has allowed us to make more accurate interpretations of both previously published and new apatite and zircon (U-Th)/He data from southern Peru that reveal rapid cooling induced by canyon incision. Our interpretations are corrected for a number of factors that were previously unexplored, including the effects of lateral changes in geothermal gradients above a subduction zone, topographic effects on thermal gradients in a high-relief landscape, thermal lag in response to changing topography, and the potential effects of early incision prior to the latest phase of incision. Although our estimates of a ~8 to 11 Ma incision onset time and $\leq$ 200 m of canyon incision prior to 14 Ma can be further refined with a better understanding of background exhumation rates through space and time, and with a more accurate representation of topographic evolution (e.g., including possible knickpoint propagation through the drainage network), our interpretations are a significant improvement over earlier estimates of the timing and magnitude of canyon incision. We anticipate that incorporating knickpoint propagation into future modeling is unlikely to lead to substantially different interpretations, as statistically acceptable fits to the whole data set assuming a simultaneous onset of incision imply that either incision onset was simultaneous along the length of the canyon, or that knickpoint propagation was relatively fast.

[54] Results presented here provide new insights into evolution of the western margin of the Altiplano in the context of a major phase of late Cenozoic uplift that has been documented across the Altiplano interior and along the eastern margin in the fold and thrust belt known as the Eastern Cordillera. Canyon incision with a magnitude up to 3.0 km starting at ~8 to 11 Ma requires contemporaneous or preceding surface uplift with at least an equal magnitude. Our data support a growing body of evidence for contemporaneous major late Cenozoic surface uplift and coupled climate change across the Central Andes.

[55] **Acknowledgments.** We thank T. Smith, K. Cornell, and J. Bradley for help with fieldwork, J. Bustamante and G.-M. Vellutino for logistical help, and W. Ouimet, J. Johnson, and K. Cook for discussions. We are grateful for detailed reviews from S. Brocklehurst and three reviewers that helped to improve the manuscript. This work was supported by the National Science Foundation Grants EAR-0409359 to K.H. and K.W. and EAR-0724656 to T.E. Additional support to T.S. was provided by the DFG-Leibnitz Center for Earth Surface and Climate Studies at the University of Potsdam.

References

Abele, G. (1989), The influence of age, climate, and relief on the preservation of volcanic landforms in the north Chilean Andes, *Bamberger Geogr. Schr.*, *11*, 45–57.

Allmendinger, R. W., and T. L. Gubbels (1996), Pure and simple shear plateau uplift, Altiplano-Puna, Argentina and Bolivia, *Tectonophysics*, *259*, 1–13, doi:10.1016/0040-1951(96)00024-8.

Alpers, C. N., and G. H. Brimhall (1988), Middle Miocene climatic-change in the Atacama Desert, northern Chile—Evidence from supergene mineralization at La-Escondida, *Geol. Soc. Am. Bull.*, *100*, 1640–1656, doi:10.1130/0016-7606(1988)100<1640:MMCCIT>2.3.CO;2.

Arndt, J., T. Bartel, E. Scheuber, and F. Schilling (1997), Thermal and rheological properties of granodioritic rocks from the central Andes, north Chile, *Tectonophysics*, *271*, 75–88, doi:10.1016/S0040-1951(96)00218-1.

Barke, R., and S. Lamb (2006), Late Cenozoic uplift of the Eastern Cordillera, Bolivian Andes, *Earth Planet. Sci. Lett.*, *249*, 350–367, doi:10.1016/j.epsl.2006.07.012.

Barnes, J. B., T. A. Ehlers, N. McQuarrie, P. B. O'Sullivan, and J. D. Pelletier (2006), Eocene to recent variations in erosion across the central Andean fold-thrust belt, northern Bolivia: Implications for plateau evolution, *Earth Planet. Sci. Lett.*, *248*, 118–133, doi:10.1016/j.epsl.2006.05.018.

Barnes, J. B., T. A. Ehlers, N. McQuarrie, P. B. O'Sullivan, and S. Tawackoli (2008), Thermochronometer record of central Andean Plateau growth, Bolivia (19.5°S), *Tectonics*, *27*, TC3003, doi:10.1029/2007TC002174.

Benfield, A. E. (1949), The effect of uplift and denudation on underground temperatures, *J. Appl. Phys.*, *20*, 66–70, doi:10.1063/1.1698238.

Berry, E. W. (1939), The fossil flora of Potosi, Bolivia, *John Hopkins Univ. Stud. Geol.*, *13*, 1–67.

Bookhagen, B., and M. R. Strecker (2008), Orographic barriers, high-resolution TRMM rainfall, and relief variations along the eastern Andes, *Geophys. Res. Lett.*, *35*, L06403, doi:10.1029/2007GL032011.

Braun, J. (2002a), Quantifying the effect of recent relief changes on age-elevation relationships, *Earth Planet. Sci. Lett.*, *200*, 331–343, doi:10.1016/S0012-821X(02)00638-6.

Braun, J. (2002b), Estimating exhumation rate and relief evolution by spectral analysis of age-elevation datasets, *Terra Nova*, *14*, 210–214, doi:10.1046/j.1365-3121.2002.00409.x.

Braun, J. (2003), Pecube: A new finite-element code to solve the 3D heat transport equation including the effects of a time-varying, finite amplitude surface topography, *Comput. Geosci.*, *29*, 787–794, doi:10.1016/S0098-3004(03)00052-9.

Braun, J., and X. Robert (2005), Quantitative constraints on the rate of landform evolution derived from low-temperature thermochrohonology, *Rev. Mineral. Geochem.*, *58*, 351–374, doi:10.2138/rmg.2005.58.13.

Cahill, T., and B. L. Isacks (1992), Seismicity and shape of the subducted Nazca plate, *J. Geophys. Res.*, *97*, 17,503–17,529, doi:10.1029/92JB00493.

Čermák, V., and L. Rybach (Eds.) (1982), Thermal properties: Landolt-Bornstein numerical data and functional relationships in science and

technology: New Series, Group V, *Geophysics and Space Research*, vol. 1, *Physical Properties of Rocks, Subvolume A*, pp. 305–371, Springer, Berlin.

Clark, M. K., M. A. House, L. H. Royden, K. X. Whipple, B. C. Burchfiel, X. Zhang, and W. Tang (2005), Late Cenozoic uplift of southeastern Tibet, *Geology*, *33*(6), 525–528, doi:10.1130/G21265.1.

Clift, P. D., I. Pecher, N. Kukowski, and A. Hampel (2003), Tectonic erosion of the Peruvian forearc, Lima Basin, by subduction and Nazca Ridge collision, *Tectonics*, *22*(3), 1023, doi:10.1029/2002TC001386.

Dodson, M. H. (1973), Closure temperature in cooling geochronological and petrological systems, *Contrib. Mineral. Petrol.*, *40*, 259–274, doi:10.1007/BF00373790.

Dortman, N. B. (1976), *Fizicheskiye Svoystva Gornykh Porod i Poleznykh Iskopaemykh (Physical Properties of Rocks and Fossil Raw Minerals)*, 527 pp., Nedra, Moscow.

Echavarria, L., R. Hernández, R. W. Allmendinger, and J. Reynolds (2003), Subandean thrust and fold belt of northwestern Argentina: Geometry and timing of the Andean evolution, *AAPG Bull.*, *87*, 965–985.

Ege, H., E. R. Sobel, E. Scheuber, and V. Jacobshagen (2007), Exhumation history of the southern Altiplano plateau (southern Bolivia) constrained by apatite fission-track thermochronology, *Tectonics*, *26*, TC1004, doi:10.1029/2005TC001869.

Ehlers, T. A. (2005), Crustal thermal processes and the interpretation of thermochronometer data, *Rev. Mineral. Geochem.*, *58*, 315–350, doi:10.2138/rmg.2005.58.12.

Ehlers, T. A., and K. A. Farley (2003), Apatite (U-Th)/He thermochronometry: Methods and applications to problems in tectonics and surface processes, *Earth Planet. Sci. Lett.*, *206*, 1–14.

Ehlers, T. A., and C. J. Poulsen (2009), Large paleoclimate influence on interpretation of Andean Plateau paleoaltimetry, *Earth Planet. Sci. Lett.*, *281*, 238–248, doi:10.1016/j.epsl.2009.02.026.

Ehlers, T. A., K. A. Farley, M. E. Rusmore, and G. J. Woodsworth (2006), Apatite (U-Th)/He signal of large magnitude and accelerated glacial erosion: Southwest British Columbia, *Geology*, *34*, 765–768, doi:10.1130/G22507.1.

Elger, K., O. Oncken, and J. Glodny (2005), Plateau-style accumulation of deformation: Southern Altiplano, *Tectonics*, *24*, TC4020, doi:10.1029/2004TC001675.

Farías, M., R. Charrier, D. Comte, J. Martinod, and G. Herail (2005), Late Cenozoic deformation and uplift of the western flank of the Altiplano: Evidence from the depositional, tectonic, and geomorphologic evolution and shallow seismic activity (northern Chile at 19 degrees 30′S), *Tectonics*, *24*, TC4001, doi:10.1029/2004TC001667.

Farley, K. A. (2000), Helium diffusion from apatite: General behavior as illustrated by Durango fluorapatite, *J. Geophys. Res.*, *105*(B2), 2903–2914, doi:10.1029/1999JB900348.

Farley, K. A. (2002), (U-Th)/He dating: Techniques, calibrations, and applications, *Rev. Mineral. Geochem.*, *47*, 819–844, doi:10.2138/rmg.2002.47.18.

Farley, K. A., R. A. Wolf, and L. T. Silver (1996), The effects of long alpha-stopping distances on (U-Th)/He ages, *Geochim. Cosmochim. Acta*, *60*(21), 4223–4229, doi:10.1016/S0016-7037(96)00193-7.

Garzione, C. N., P. Molnar, J. C. Libarkin, and B. J. MacFadden (2006), Rapid late Miocene rise of the Bolivian Altiplano: Evidence for removal of mantle lithosphere, *Earth Planet. Sci. Lett.*, *241*, 543–556, doi:10.1016/j.epsl.2005.11.026.

Ghosh, P., C. N. Garzione, and J. M. Eiler (2006), Rapid uplift of the Altiplano revealed through C-13-O-18 bonds in paleosol carbonates, *Science*, *311*(5760), 511–515, doi:10.1126/science.1119365.

Graham, A., K. M. Gregory-Wodzicki, and K. L. Wright (2001), Studies in neotropical paleobotany. XV. A Mio-Pliocene palynoflora from the Eastern Cordillera, Bolivia: Implications for the uplift history of the central Andes, *Am. J. Bot.*, *146*(3), 813–826.

Gregory-Wodzicki, K. M. (2000), Uplift history of the central and northern Andes: A review, *Geol. Soc. Am. Bull.*, *112*, 1091–1105, doi:10.1130/0016-7606(2000)112<1091:UHOTCA>2.3.CO;2.

Gubbels, T. L., B. L. Isacks, and E. Farrar (1993), High-level surfaces, plateau uplift, and foreland development, Bolivian central Andes, *Geology*, *21*(8), 695–698, doi:10.1130/0091-7613(1993)021<0695:HLSPUA>2.3.CO;2.

Haenel, R., L. Rybach, and L. Stegena (1988), *Handbook of Terrestrial Heat-Flow Density Determination: With Guidelines and Recommendations of the International Heat Flow Commission*, Kluwer Acad., Dordrecht, Netherlands.

Hampel, A. (2002), The migration history of the Nazca Ridge along the Peruvian active margin: A re-evaluation, *Earth Planet. Sci. Lett.*, *203*, 665–679, doi:10.1016/S0012-821X(02)00859-2.

Hamza, V. M., and M. Munoz (1996), Heat flow map of South America, *Geothermics*, *25*(6), 599–646, doi:10.1016/S0375-6505(96)00025-9.

Hamza, V. M., F. J. S. S. Dias, A. J. L. Gomes, and Z. G. D. Terceros (2005), Numerical and functional representations of regional heat flow in South America, *Phys. Earth Planet. Inter.*, *152*(4), 223–256.

Henry, S. G. (1981), Terrestrial heat flow overlying the Andean subduction zone, Ph.D. thesis, Univ. of Michigan, Ann Arbor.

Henry, S. G., and H. N. Pollack (1988), Terrestrial heat-flow above the Andean subduction zone in Bolivia and Peru, *J. Geophys. Res.*, *93*(B12), 15,153–15,162, doi:10.1029/JB093iB12p15153.

Herman, F., J. Braun, and W. J. Dunlap (2007), Tectonomorphic scenarios in the southern Alps of New Zealand, *J. Geophys. Res.*, *112*, B04201, doi:10.1029/2004JB003472.

Hoke, G. D., and C. N. Garzione (2008), Paleosurfaces, paleoelevation, and the mechanisms for the latest Miocene topographic development of the Altiplano Plateau, *Earth Planet. Sci. Lett.*, *271*, 192–201, doi:10.1016/j.epsl.2008.04.008.

Hoke, G. D., B. L. Isacks, T. E. Jordan, N. Blanco, A. J. Tomlinson, and J. Ramezani (2007), Geomorphic evidence for post-10 Ma uplift of the western flank of the central Andes 18°30′–22°S, *Tectonics*, *26*, TC5021, doi:10.1029/2006TC002082.

Horton, B. K. (2005), Revised deformation history of the central Andes: Inferences from Cenozoic foredeep and intermontane basins of the Eastern Cordillera, Bolivia, *Tectonics*, *24*, TC3011, doi:10.1029/2003TC001619.

Hourigan, J. K., P. W. Reiners, and M. T. Brandon (2005), U-Th zonation-dependent alpha-ejection in (U-Th)/He chronometry, *Geochim. Cosmochim. Acta*, *69*(13), 3349–3365, doi:10.1016/j.gca.2005.01.024.

House, M. A., B. P. Wernicke, and K. A. Farley (1998), Dating topographic uplift of the Sierra Nevada, CA, using apatite (U-Th)/He ages, *Nature*, *396*, 66–69, doi:10.1038/23926.

House, M. A., B. P. Wernicke, and K. A. Farley (2001), Paleo-geomorphology of the Sierra Nevada, California, from (U-Th)/He ages in apatite, *Am. J. Sci.*, *301*, 77–102, doi:10.2475/ajs.301.2.77.

Houston, J., and A. J. Hartley (2003), The central Andean west-slope rainshadow and its potential contribution to the origin of hyper-aridity in the Atacama desert, *Int. J. Climatol.*, *23*(12), 1453–1464, doi:10.1002/joc.938.

Huntington, K. W., T. A. Ehlers, K. V. Hodges, and D. M. Whipp Jr. (2007), Topography, exhumation pathway, age uncertainties, and the interpretation of thermochronometer ages, *Tectonics*, *26*, TC4012, doi:10.1029/2007TC002108.

INGEMMET (2001), Mapa Geológico del cuadrángulo de Caravelí, Ocoña, La Yesera, y Chuquibamba, scale 1:100,000, Lima.

Isacks, B. L. (1988), Uplift of the central Andean Plateau and bending of the Bolivian Orocline, *J. Geophys. Res.*, *93*(B4), 3211–3231.

Jaillard, E., and P. Soler (1996), Cretaceous to early Paleogene tectonic evolution of the northern Central Andes (0–18°S) and its relations to geodynamics, *Tectonophysics*, *259*, 41–53, doi:10.1016/0040-1951(95)00107-7.

Jordan, T. E., B. L. Isacks, R. W. Allmendinger, J. A. Brewer, V. A. Ramos, and C. J. Ando (1983), Andean tectonics related to geometry of subducted Nazca Plate, *Geol. Soc. Am. Bull.*, *94*(3), 341–361, doi:10.1130/0016-7606(1983)94<341:ATRTGO>2.0.CO;2.

Jordan, T. E., C. Mpodozis, N. Blanco, G. D. Hoke, and P. L. Nester (2006), Surface uplift of the western slope of the Puna segment of the central Andean Plateau, *Geol. Soc. Am. Abstr. Programs*, *2*, p. 86.

Kappelmeyer, O., and R. Haenel (1974), *Geothermics With Special Reference to Applications*, 238 pp., Gebrüder Borntraeger, Berlin.

Kennan, L., S. Lamb, and L. Hoke (1997), High altitude palaeosurfaces in the Bolivian Andes: Evidence for Late Cenozoic surface uplift, in *Paleosurfaces: Recognition, Reconstruction and Paleoenvironmental Interpretation*, edited by M. Widdowson, *Geol. Soc. Spec. Publ.*, *120*, 307–324.

Klein, A. G., G. O. Seltzer, and B. L. Isacks (1999), Modern and last local glacial maximum snowlines in the central Andes of Peru, Bolivia and northern Chile, *Quat. Sci. Rev.*, *18*, 63–84, doi:10.1016/S0277-3791(98)00095-X.

Kober, F., S. Ivy-Ochs, F. Schlunegger, H. Baur, P. W. Kubik, and R. Wieler (2007), Denudation rates and a topography-driven rainfall threshold in northern Chile: Multiple cosmogenic nuclide data and sediment yield budgets, *Geomorphology*, *83*, 97–120, doi:10.1016/j.geomorph.2006.06.029.

Lees, C. H. (1910), On the shape of the isogeotherms under mountain range in radio-active districts, *Proc. R. Soc. London, Ser. A*, *83*, 339–346, doi:10.1098/rspa.1910.0022.

Lenters, J. D., and K. H. Cook (1995), Simulation and diagnosis of the regional summertime precipitation climatology of South America, *J. Clim.*, *8*, 2988–3005, doi:10.1175/1520-0442(1995)008<2988:SADOTR>2.0.CO;2.

Lenters, J. D., and K. H. Cook (1997), On the origin of the Bolivian high and related circulation features of the South American climate, *J. Atmos. Sci.*, *54*, 656–677, doi:10.1175/1520-0469(1997)054<0656:OTOOTB>2.0.CO;2.

Li, C., and A. L. Clark (1994), Tectonic effects of the subducting Nazca Ridge on the southern Peru continental-margin, *Mar. Pet. Geol.*, *11*(5), 575–586, doi:10.1016/0264-8172(94)90069-8.

Machare, J., and L. Ortlieb (1992), Plioquaternary vertical motions and the subduction of the Nazca Ridge, central coast of Peru, *Tectonophysics*, *205*, 97–108, doi:10.1016/0040-1951(92)90420-B.

Mancktelow, N. S., and B. Grasemann (1997), Time-dependent effects of heat advection and topography on cooling histories during erosion, *Tectonophysics*, *270*, 167–195, doi:10.1016/S0040-1951(96)00279-X.

McQuarrie, N. (2002), The kinematic history of the central Andean fold-thrust belt, Bolivia: Implications for building a high plateau, *Geol. Soc. Am. Bull.*, *114*, 950–963, doi:10.1130/0016-7606(2002)114<0950:TKHOTC>2.0.CO;2.

McQuarrie, N., J. B. Barnes, and T. A. Ehlers (2008), Geometric, kinematic, and erosional history of the central Andean Plateau, Bolivia (15–17°S), *Tectonics*, *27*, TC3007, doi:10.1029/2006TC002054.

Mel'nikova, N. V., V. V. Rzhevskogo, and M. M. Protod'yakonova (1975), *Spravochnik (Kadastr) Fisicheskikh Svoystv Gornykh Porod (Handbook [Registry] of Physical Properties of Rocks)*, 279 pp., Nedra, Moscow.

Mercier, J. L., M. Sébrier, A. Lavenu, J. Cabrera, O. Bellier, J. F. Dumont, and J. Machare (1992), Changes in the tectonic regime above a subduction zone of Andean type: The Andes of Peru and Bolivia during the Pliocene-Pleistocene, *J. Geophys. Res.*, *97*(B8), 11,945–11,982, doi:10.1029/90JB02473.

Moiseenko, U. I., L. S. Sokolova, and V. E. Istomin (1970), *Elektricheskie I Teplovye Svoystva Gornykh Porod v Usloviyakh Normal'nykh I Vysokikh Temperatur I Davleniy (Electrical and Thermal Properties of Rocks under Normal and High Temperatures and Pressures)*, 66 pp., Sibirskoe Otdelenie, Nauka, Novosibirsk, Russia.

Mukasa, S. B. (1986), Zircon U-Pb ages of super-units in the Coastal batholith, Peru: Implications for magmatic and tectonic processes, *Geol. Soc. Am. Bull.*, *97*(2), 241–254, doi:10.1130/0016-7606(1986)97<241:ZUAOSI>2.0.CO;2.

Nester, P. L. (2008), Basin and paleoclimate evolution of the Pampa del Tamarugal Forearc Valley, Atacama Desert, northern Chile, Ph.D. thesis, 253 pp., Cornell Univ., Ithaca, New York.

Ouimet, W. (2007), Dissecting the eastern margin of the Tibetan Plateau: A study of landslides, erosion and river incision in a transient landscape, Ph.D. thesis, 197 pp., Mass. Inst. of Technol., Cambridge.

Pardo-Casas, F., and P. Molnar (1987), Relative motion of the Nazca (Farallon) and South American plates since late Cretaceous time, *Tectonics*, *6*(3), 233–248, doi:10.1029/TC006i003p00233.

Pearson, E. S., and H. O. Hartley (1966), *The Biometrika Tables for Statisticians*, 3rd ed., Biometrika, Cambridge, U. K.

Pollack, H. N. (1982), The heat flow from the continents, *Annu. Rev. Earth Planet. Sci.*, *10*, 459–481, doi:10.1146/annurev.ea.10.050182.002331.

Quade, J., C. Garzione, and J. Eiler (2007), Paleoelevation reconstruction using pedogenic carbonates, *Rev. Mineral. Geochem.*, *66*, 53–87, doi:10.2138/rmg.2007.66.3.

Rech, J. A., B. S. Currie, G. Michalski, and A. M. Cowan (2006), Neogene climate change and uplift in the Atacama Desert, Chile, *Geology*, *34*(9), 761–764, doi:10.1130/G22444.1.

Reiners, P. W., T. L. Spell, S. Nicolescu, and K. A. Zanetti (2004), Zircon (U-Th)/He thermochronology: He diffusion and comparisons with 40Ar/39Ar dating, *Geochim. Cosmochim. Acta*, *68*(8), 1857–1887, doi:10.1016/j.gca.2003.10.021.

Reiners, P. W., T. A. Ehlers, and P. K. Zeitler (2005), Past, present, and future of thermochronology, in *Thermochronology*, edited by P. W. Reiners and T. A. Ehlers, *Rev. Mineral. Geochem.*, *58*, 1–18.

Rodwell, M. J., and B. J. Hoskins (2001), Subtropical anticyclones and summer monsoons, *J. Clim.*, *14*, 3192–3211, doi:10.1175/1520-0442(2001)014<3192:SAASM>2.0.CO;2.

Roperch, P., T. Sempere, O. Macedo, C. Arriagada, M. Fornari, C. Tapia, M. García, and C. Laj (2006), Counterclockwise rotation of late Eocene-Oligocene forearc deposits in southern Peru and its significance for oroclinal bending in the central Andes, *Tectonics*, *25*, TC3010, doi:10.1029/2005TC001882.

Schildgen, T. F. (2008), Surface uplift, fluvial incision, and geodynamics of plateau evolution, from the western margin of the central Andean plateau, Ph.D. thesis, 154 pp., Mass. Inst. of Technol., Cambridge.

Schildgen, T. F., K. V. Hodges, K. X. Whipple, P. W. Reiners, and M. S. Pringle (2007), Uplift of the western margin of the Andean plateau revealed from canyon incision history, southern Peru, *Geology*, *35*(6), 523–526, doi:10.1130/G23532A.1.

Schildgen, T. F., K. V. Hodges, K. X. Whipple, M. S. Pringle, M. Van Soest, and K. Cornell (2009), Late Cenozoic structural and tectonic development of the western margin of the Central Andean Plateau in southwest Peru, *Tectonics*, *28*, TC4007, doi:10.1029/2008TC002403.

Schlunegger, F., G. Zeilinger, A. Kounov, F. Kober, and B. Husser (2006), Scale of relief growth in the forearc of the Andes of northern Chile (Arica latitude, 18 degrees S), *Terra Nova*, *18*(3), 217–223, doi:10.1111/j.1365-3121.2006.00682.x.

Schön, J. H. (1996), *Physical Properties of Rocks: Fundamentals and Principles of Petrophysics*, 583 pp., Pergamon, Tarrytown, N. Y.

Sébrier, M., and P. Soler (1991), Tectonics and magmatism in the peruvian Andes from late Oligocene time to the present, in *Andean Magmatism and its Tectonic Setting*, edited by R. S. Harmon and C. W. Rapela, *Spec. Pap. Geol. Soc. Am.*, *265*, 259–278.

Sempere, T., M. Fornari, J. Acosta, A. Flores, J. Jacay, D. Peña, P. Roperch, and E. Taipe (2004), Estratigrafía, geochronología, paleogeografía y paleotectónica de los dépositos de antearco del sur del Perú, paper presented at XII Congreso Peruano de Geología, Soc. Geol. Del Perú, Lima.

Shuster, D. L., T. A. Ehlers, M. R. Rusmore, and K. A. Farley (2005), Rapid glacial erosion at 18 Ma revealed by 4He/3He thermochronometry, *Science*, *310*, 1668–1670, doi:10.1126/science.1118519.

Singewald, J. T., and E. W. Berry (1922), The geology of the Corocoro copper district of Bolivia, *John Hopkins Univ. Stud. Geol.*, *1*, 1–117.

Somoza, R. (1998), Updated Nazca (Farallon): South America relative motions during the last 40 My: Implications for mountain building in the central Andean region, *J. South Am. Earth Sci.*, *11*(3), 211–215, doi:10.1016/S0895-9811(98)00012-1.

Spotila, J. A., K. A. Farley, and K. Sich (1998), Uplift and erosion of the San Bernardino Mountains associated with transpression along the San Andreas fault, California, as constrained by radiogenic helium thermochronometry, *Tectonics*, *17*(3), 360–378, doi:10.1029/98TC00378.

Springer, M. (1999), Interpretation of heat-flow density in the central Andes, *Tectonophysics*, *306*, 377–395, doi:10.1016/S0040-1951(99)00067-0.

Springer, M., and A. Förster (1998), Heat-flow density across the central Andean subduction zone, *Tectonophysics*, *291*, 123–139, doi:10.1016/S0040-1951(98)00035-3.

Stern, C. R. (2004), Active Andean volcanism: Its geologic and tectonic setting, *Rev. Geol. Chile*, *31*, 161–206.

Strecker, M. R., P. Cerveny, A. L. Bloom, and D. Malizia (1989), Late Cenozoic tectonism and landscape development in the foreland of the Andes: Northern Sierras Pampeanas, Argentina, *Tectonics*, *8*, 517–534, doi:10.1029/TC008i003p00517.

Strecker, M. R., R. N. Alonso, B. Bookhagen, B. Carrapa, G. E. Hilley, E. R. Sobel, and M. H. Trauth (2007), Tectonics and climate of the southern central Andes, *Annu. Rev. Earth Planet. Sci.*, *35*, 747–787, doi:10.1146/annurev.earth.35.031306.140158.

Stüwe, K., L. White, and R. Brown (1994), The influence of eroding topography on steady-state isotherms: Application to fission-track analysis, *Earth Planet. Sci. Lett.*, *124*, 63–74, doi:10.1016/0012-821X(94)00068-9.

Takahashi, K., and D. S. Battisti (2007), Processes controlling the mean tropical Pacific precipitation pattern. Part 1: The Andes and the Eastern Pacific ITCZ, *J. Clim.*, *20*, 3434–3451, doi:10.1175/JCLI4198.1.

Thouret, J.-C., G. Wörner, Y. Gunnell, B. Singer, X. Zhang, and T. Souriot (2007), Geochronologic and stratigraphic constraints on canyon incision and Miocene uplift of the central Andes in Peru, *Earth Planet. Sci. Lett.*, *263*, 151–166, doi:10.1016/j.epsl.2007.07.023.

Turcotte, D. L., and G. Schubert (1982), *Geodynamics, Applications of Continuum Physics to Geological Problems*, 450 pp., John Wiley, New York.

Uyeda, S., T. Wantanabe, Y. Ozasayama, and K. Ibaragi (1980), Report of heat flow measurements in Peru and Ecuador, *Bull. Earthquake Res. Inst.*, *55*, 55–74.

Victor, P., O. Oncken, and J. Glodny (2004), Uplift of the western Altiplano plateau: Evidence from the Precordillera between 20° and 21°S (northern Chile), *Tectonics*, *23*, TC4004, doi:10.1029/2003TC001519.

von Huene, R., and C. R. Ranero (2003), Subduction erosion and basin friction along the sediment starved convergent margin off Antofagasta, Chile, *J. Geophys. Res.*, *108*(B2), 2079, doi:10.1029/2001JB001569.

Vorsteen, H.-D., and R. Schellschmidt (2003), Influence of temperature on thermal conductivity, thermal capacity and thermal diffusivity for different types of rock, *Phys. Chem. Earth*, *28*, 499–509.

Whipple, K. X., and G. E. Tucker (1999), Dynamics of the stream-power river incision model: Implications for height limits of mountain ranges, landscape response timescales, and research needs, *J. Geophys. Res.*, *104*, 17,661–17,674, doi:10.1029/1999JB900120.

Whipple, K. X., and G. E. Tucker (2002), Implications of sediment-flux-dependent river incision models for landscape evolution, *J. Geophys. Res.*, *107*(B2), 2039, doi:10.1029/2000JB000044.

Wolf, R. A., K. A. Farley, and D. M. Kass (1998), Modeling of the temperature sensitivity of the apatite (U-Th)/He thermochronometer, *Chem. Geol.*, *148*(1–2), 105–114, doi:10.1016/S0009-2541(98)00024-2.

Wörner, G., D. Uhlig, I. Kohler, and H. Seyfried (2002), Evolution of the West Andean Escarpment at 18°S (N. Chile) during the last 25 Ma:

Uplift, erosion and collapse through time, *Tectonophysics*, *345*(1–4), 183–198, doi:10.1016/S0040-1951(01)00212-8.

Yamano, M., and S. Uyeda (1990), Heat-flow studies in the Peru Trench subduction zone, *Proc. Ocean Drill. Program, Sci. Results*, *112*, 653–661.

T. A. Ehlers, Institut für Geowissenschaften, Universität Tübingen, Wilhelmstr.56, D-72074 Tübingen, Germany. (tehlers@umich.edu)

K. V. Hodges, M. C. van Soest, and K. X. Whipple, School of Earth and Space Exploration, Arizona State University, PO Box 871404, Tempe, AZ 85287, USA. (kvhodges@asu.edu; matthijs.vansoest@asu.edu; kxw@asu.edu)

T. F. Schildgen, Institut für Geowissenschaften, University of Potsdam, Karl-Liebknecht-Str. 24, Haus 27, D-14476 Potsdam, Germany. (tschild@uni-potsdam.de)

D. M. Whipp Jr., Géosciences Rennes, Université de Rennes 1, 263 ave. du General Leclerc, F-35042 Rennes CEDEX, France. (david.whipp@univ-rennes1.fr)